Data-space cross-validation of mantle structure in global tomographic models underneath the Pacific Ocean

Mathurin D. Wamba[1], Frederik J. Simons[1], and Jessica C. E. Irving[2]

[1]*Department of Geosciences, Princeton University, Princeton, NJ 08544, USA.*
  Now at: *Institute of Geological Sciences, Universität Bern, 3012 Bern. CH. E-mail:* mathurin.dongmowamba@unibe.ch
[2]*School of Earth Sciences, University of Bristol, Bristol, BS8 1RJ, UK.*

28 January 2025

S U M M A R Y

Seismic tomography is a principal method for studying mantle structure, but imaging of Earth's wavespeed anomalies is conditioned by seismic wave sampling. Global models use misfit criteria that may strive for balance between portions of the data set but can leave important regional domains underserved. We evaluate two full-waveform global tomography wavespeed models, GLAD-M25 and SEMUCB-WM1, in the mantle below the Pacific Ocean. The region of the South Pacific Superswell contains multiple hotspots which may be fed by plumes anchored in the Large Low Shear-Velocity Province at the base of the mantle. The uneven distribution of seismic receivers worldwide leaves several candidate plumes beneath various hotspots poorly resolved. We assess the regional quality of GLAD-M25 relative to its global performance using a partition of the seismic waveform data used in its construction. We evaluate synthetic waveforms computed using the spectral-element method to determine how well they fit the data according to a variety of criteria measured across multiple seismic phases and frequency bands. The distributions of travel-time anomalies that remain in GLAD-M25 are wider for trans-Pacific paths than globally, suggesting comparatively insufficiently resolved seismic velocity structure in the region of interest. Hence, Pacific-centered regional inversions, based on (augmented) subsets of the global data set have the potential to enhance the resolution of velocity structure. We compare GLAD-M25 and SEMUCB-WM1 by cross-validation with a new, independent, data set. Our results reveal that short- and long-wavelength structure is captured differently by the two models. Our findings lead us to recommend focusing future model iteration on and around the Pacific Superswell and adding data that sample new corridors, especially using ocean sensors, to better constrain seismic velocity structure in this area of significant geodynamic complexity.

Key words: Seismic tomography, Computational seismology, Pacific Ocean

1 INTRODUCTION

Mantle upwellings play a vital role in Earth processes (Koppers et al. 2021), and when they take the form of narrow mantle plumes, they provide an essential window into the structure, composition, and dynamics of Earth's deep interior (Weis et al. 2023). Most volcanic hotspots are located in the oceans (Sleep 1990; Courtillot et al. 2003; King & Adam 2014), which cover two-thirds of Earth's surface. It is challenging to deploy seismic stations around ocean islands to increase imaging aperture (Wolfe et al. 2009; Maguire et al. 2018), which has led to biases in seismic imaging of mantle plumes compared to subduction zones (Montelli et al. 2006; Nolet et al. 2007). The latter have been rather well imaged by models (van der Hilst et al. 1993; Grand et al. 1997; Fukao et al. 2001) that have received sustained data addition and methodological improvement (Li et al. 2008; Lu et al. 2019; Obayashi et al. 2013; Sigloch & Mihalynuk 2013). Observing seismic waves beneath the oceans requires specialized equipment and sensors such as ocean-bottom seismometers (Collins et al. 2001; Kohler et al. 2020), anchored (Slack et al. 1999; Sukhovich et al. 2014) or floating (Sukhovich et al. 2015; Simon et al. 2021) hydrophones at mid-column depths.

Several global tomographic models (Zhao 2004; Kustowski et al. 2008; Ritsema et al. 2011; French & Romanowicz 2015; Bozdağ et al. 2016; Lei et al. 2020) developed using different methodologies have provided evidence of broad low shear-wave speed zones beneath several major hotspots, providing insight into the structure of Earth's mantle plumes (Ritsema et al. 2021; Lu & Rudolph 2024). The rise of buoyant plumes may be influenced by flow and basal structure within the mantle (Steinberger 2000; Austermann et al. 2014; Nolet et al. 2007), and compositional and rheological properties (Dannberg & Sobolev 2015; Davaille et al. 2018; Gülcher et al. 2022), making their large-scale
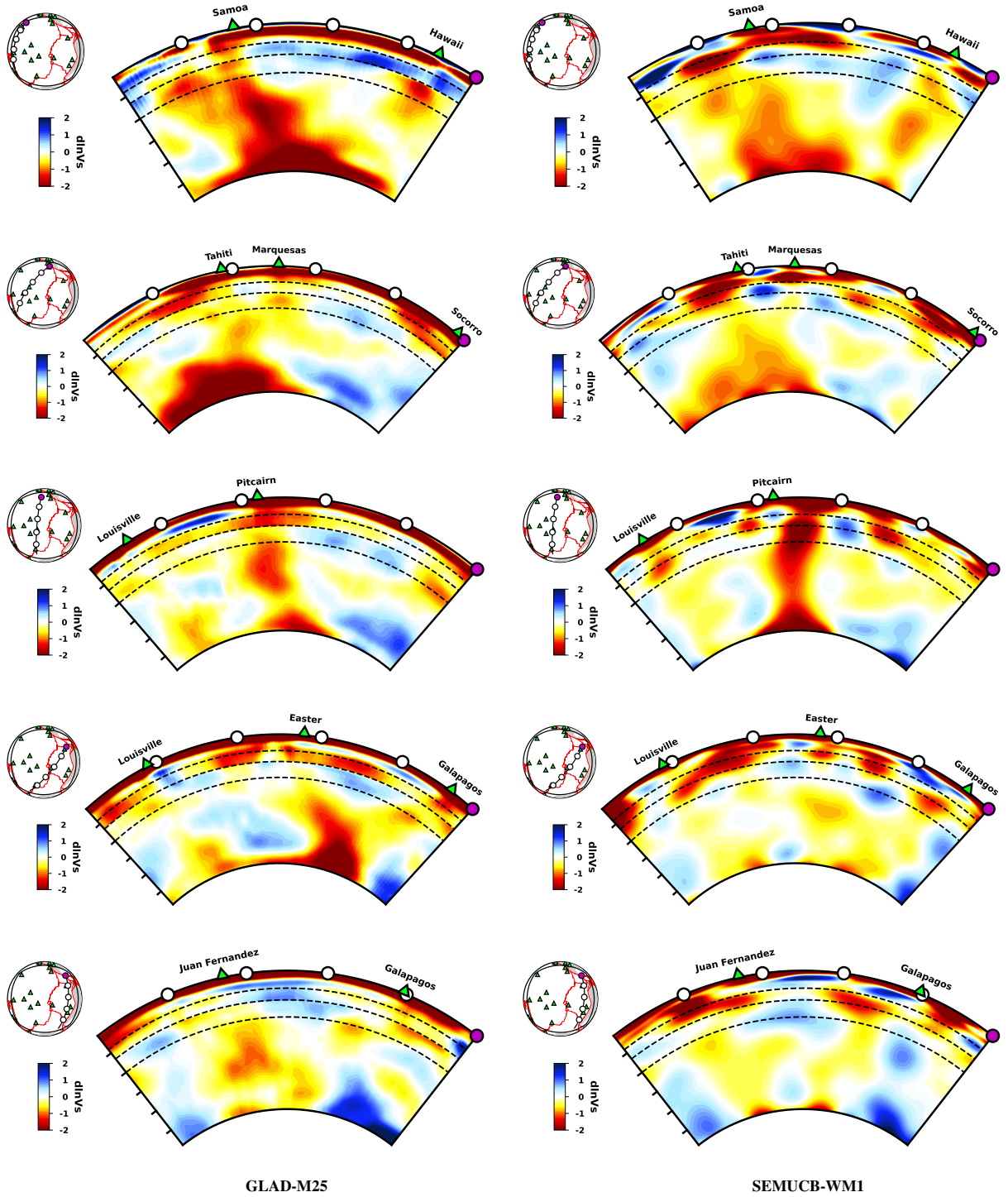
Figure 1. Relative mantle shear-wave speed anomalies (dlnVs, per cent) in global tomography models GLAD-M25 *(left column)* and SEMUCB-WM *(right)*. Cross-sections follow great-circle paths shown in the map inserts. Green triangles indicate hotspots (see Steinberger 2000). Dashed black lines mark 410, 660, and 1000 km depth. Both models agree on the presence of mantle plumes below Samoa *(top row)* and Pitcairn *(middle)*, rising from the core-mantle boundary. Below Tahiti and the Marquesas *(second row)* the low and high velocity anomalies are similarly shaped and positioned in both models, although they are mismatched in amplitude. Between Easter Island and the Galápagos *(fourth row)*, GLAD-M25 shows a low-velocity anomaly anchored at the core-mantle boundary. No comparable structure is present in SEMUCB-WM1. Beneath Louisville *(middle and fourth rows)*, GLAD-M25 has mantle structure that is inconsistent with SEMUCB-WM1. Directly beneath Galápagos *(bottom)*, both models show significant fast velocity anomalies near the core-mantle boundary.

structure more complex than in the canonical Morgan (1971) hypothesis, which continues to generate lively debate (Foulger 2002, 2021). Seismic anisotropy is an important indicator of mantle flow (Fouch et al. 2001; Gaherty 2001; Benoit et al. 2013; Faccenda & VanderBeek 2023), but direct sinference is significantly complicated by the mechanisms of microstructural fabric formation, and, in particular, the presence of water and partial melt (Park & Levin 2002; Karato et al. 2008). Here, we only consider isotropic elastic wave speed variations.

Intricate plume structures comprising ponding zones (Nolet et al. 2006; Wamba et al. 2021) and branching networks have been imaged, e.g., in the Indian Ocean beneath La Réunion (Tsekhmistrenko et al. 2021; Wamba et al. 2023) and in the Antarctic Rift System beneath Marie Byrd Land (e.g., Hansen et al. 2014). Beneath the Central Pacific around Hawaii, models based on a variety of observables suggest that seismically slow material may have accumulated in the mid-mantle (Shen et al. 2003; Yu et al. 2018; Zhang et al. 2023). These apparently different plume morphologies and flow regimes may imply different scenarios for the evolution of Earth's silicate mantle. Understanding mantle evolution maps onto questions about specific seismic models, two of which we compare in this paper.

Seismological model and data comparisons may take many forms (Ritsema & Lekić 2020; Moulik et al. 2022). Numerous authors have conducted detailed inter-model evaluations, on the basis of a variety of measures which are relatively straightforward to obtain from images, both planforms and cross-sections. These include correlation-based comparisons and confrontations with geodynamic models (e.g. Jordan et al. 1993; Rudolph et al. 2015), cross-filtered to account for the tomographic resolution operator (e.g., Schuberth et al. 2009; Su et al. 2023), vote-mapping based consistency checks (e.g., Shephard et al. 2017), consensus-based cluster analyses (e.g., Lekić et al. 2012; Cottaar & Lekić 2016), spectral-domain cross-model comparisons and grand averaging to an agreed-upon "best" model (e.g., Becker & Boschi 2002), and statistical measures characterizing the relative distributions of anomalies (e.g., Hernlund & Houser 2008). In contrast, intra-model comparisons and direct data evaluations (Ritsema et al. 2002; Bozdağ & Trampert 2010), have been relatively rare. While the computational cost of data-space cross-validation is higher, it can lead to a more focused identification of the geographical areas that are most in need of, or present most promise for, improvement.

1.1 GLAD-M25 and SEMUCB-WM1, two full-waveform global seismic models

The two global tomography models that we interrogate are GLAD-M25 (Lei et al. 2020) and SEMUCB-WM1 (French & Romanowicz 2014, 2015). They are readily available for analysis (Trabant et al. 2012; Ciardelli et al. 2022). Fig. 1 shows a variety of their cross-sections that can be mapped onto specific science questions. As we will not be able to address each individually, our focus will be on an overall assessment of model resolution and data fit within and across both models, as a prerequisite for more detailed interpretive work.

Seismic tomography model GLAD-M25 (Lei et al. 2020) was based on adjoint full-waveform inversion (Tromp et al. 2005; Liu & Tromp 2008; Liu & Gu 2012) of global seismic data from 1,480 earthquakes recorded at 11,800 seismic stations, modeled (down to 17 s period) using a spectral-element approach on a polynomial node grid (SPECFEM3D_GLOBE, Komatitsch et al. 2000). Shown in Fig. 1 (*left column*), are cross-sections through the shear-wave anomaly model. GLAD-M25 improved upon first-generation model GLAD-M15 (Bozdağ et al. 2016), itself an update of S362ANI by Kustowski et al. (2008), which incorporated crustal model CRUST2.0 (Bassin et al. 2000). The one-dimensional attenuation model was unchanged from the QL6 profile (Durek & Ekström 1996). Radial anisotropy in GLAD-M25 is confined to the upper mantle. Despite the amount of data that was assimilated (millions of individual measurement windows) and the overall high model quality, structure below several hotspots in the Pacific (e.g., Louisville, Marquesas, Easter, Tahiti, Galápagos), remains challenging to interpret. Other hotspots in the region (e.g., Samoa and Pitcairn) do show evidence for whole-mantle plumes rising from the core-mantle boundary (CMB) to the upper mantle. Even in regions with adequate data coverage, poorly constrained structure may be ascribed to a combination of source uncertainty (Sawade et al. 2022) and an incomplete model parameterization, including the lack of azimuthal anisotropy (Becker et al. 2003), inherited topography on internal discontinuities (Burky et al. 2023), unaccounted-for heterogeneous wavespeed attenuation (Lei et al. 2020), and other "approximations and arbitrary choices" (Valentine & Trampert 2015).

Shown in Fig. 1 (*right column*), seismic tomography shear-velocity model SEMUCB-WM1 (French & Romanowicz 2014, 2015) is also a whole-mantle model developed using full-waveform inversion (Lekić & Romanowicz 2011). The forward seismic wavefield of 273 events at over 500 stations was computed (down to 32 s period) using a spectral-element method (CSEM, Capdeville et al. 2003), with a parameterization by spherical splines (Wang & Dahlen 1995) laterally and B-splines vertically. The inverse problem is solved using a Gauss-Newton optimization approach, where gradient and Hessian kernels were recomputed at each iteration using non-linear asymptotic mode coupling theory (NACT, Li & Romanowicz 1995). The starting model was SEMum2 (French et al. 2013) for the upper mantle and SAW24B16 (Mégnin & Romanowicz 2000) for the lower mantle, both computed by full-waveform inversion, the former using CSEM and the latter using NACT for forward wavefield computations. Unlike with GLAD-M25, radial anisotropy is included throughout the mantle. The one-dimensional attenuation model QL6 (Durek & Ekström 1996) was held fixed. The three-dimensional radially anisotropic homogenized crust was updated at each iteration to fit a set of Love and Rayleigh wave dispersion curves in the period range 20–60 s.

Valentine & Trampert (2015) point out the dangers of computing sensitivity kernels using a different theoretical basis to that employed for forward modelling. This may indeed be problematic when the starting model is far away from the (unknown) target model. However, SEMUCB-WM1 was constructed progressively, starting at very long periods and long wavelengths, and using a one-dimensional model that fits a large global data set of teleseismic travel times (Lekić & Romanowicz 2011). Progressively, shorter wavelengths and a larger number of wave packets were added, giving rise to emerging three-dimensional structure. In other words, the starting model for SEMUCB-WM1 has robust long-wavelength features, justifying the approach taken. The misfit function, computed using spectral-element modeling, is accurate, while errors in the gradient are of second order, see Tarantola (1986) and Lekić & Romanowicz (2011), their Appendix A. Hence the gradient will point non-erratically towards decreasing misfit.

Note that the automatic selection of windows was carried out by FLEXWIN (Maggi et al. 2009) in both models, but the selection criteria in GLAD-M25 differ from those used in the construction of SEMUCB-WM1 (e.g., Romanowicz 2023). More details about the differences in the construction of models SEMUCB-WM1 and GLAD-M25 can be found in Romanowicz (2023).
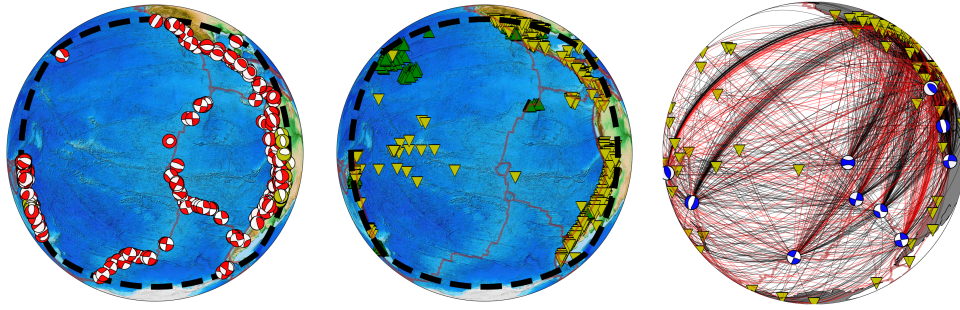
Figure 2. (*Left*) Focal mechanisms of 453 sources from the GLAD-M25 data set falling within our region of interest, dashed in black. White-yellow sources are over 300 km deep, white-red mechanisms occur at shallower depths. (*Middle*) 380 land stations (yellow, inverted triangles) and 117 ocean-bottom seismometers (green triangles). (*Right*) Stations, earthquake locations and mechanisms, and their great-circle paths from the independent data set that we used for cross-validation of global seismic models GLAD-M25 and SEMUCB-WM1. Paths corresponding to travel-time anomalies exceeding ± 5 s are rendered red.

1.2   Objectives of this paper

We formulate the two objectives of this paper. First, to assess the need for regional model improvement within GLAD-M25 across our Pacific area of interest, e.g., by continued full-waveform inversion of subsets of the data that cover the target region and/or by the addition of new, especially oceanic, data. Second, to compare GLAD-M25 model with SEMUCB-WM1 in the region of interest. We do not seek to rank the two models in this work: both models are numerically optimized "best" versions of the truth as revealed by their data sets, but it is not *a priori* clear whether the match between observed and simulated data influenced by model structure within a specific regional domain of interest is as good as, better, or worse, than the overall level of fit reached by globally averaged evaluation. These questions, involving the probabilistic mapping between data and model covariance spaces, are of a very general nature (Tarantola 2005; Valentine & Trampert 2012).

To attain our objectives, we conduct two data-space assessments by comparing metrics relating observations to synthetic data simulated in both models. Our first assessment focuses on a regional-versus-global evaluation of misfit via comparisons of the travel-time anomaly distribution for a variety of wave types that are sensitive to the target region. As the region of interest we use a portion of the cubed sphere (Ronchi et al. 1996), delineated in black in Fig. 2. To compare GLAD-M25 with SEMUCB-WM1, we assemble an independent, smaller, data set, compute wavefields in the same Pacific region enclosing Polynesia, calculate the similarities between synthetics and observations, and make histograms of relative travel-time anomalies to ascertain whether apparent differences in model structure are warranted by the data.

This work is structured as follows. We isolate the Pacific region under investigation and identify, from the database underlying the GLAD-M25 model, seismic event-station pairs that fall within the target region, and compile their observed and synthetic waveforms. We discuss the metrics by which we relate the observed to the predicted data. We calculate histograms of relative travel-time anomalies within GLAD-M25 across different data categories (e.g., body and long-period surface waves, all three seismogram components) and period bands, contrasting the regional subset with the global values to allow for model intra-comparison. We next perform model inter-comparisons between GLAD-M25 and SEMUCB-WM1 using similar metrics, but this time on the basis of an independent data set. We use the word 'independent' to mean that the new data set was not involved in the construction of either model. While these data are of the same seismological type, and receive the same treatment and processing as those used to build GLAD-M25 and SEMUCB-WM1, the synthetic waveforms are newly computed and compared. Both comparisons shed light on the relative quality of both models, and lead to recommendations for further inversions based on long-period waveforms or travel-times that may ultimately help us to enhance imaging of structure beneath the Pacific.

2   DATA AND METHODS

For the model intra-comparison, i.e., to assess model quality at the regional scale of the Pacific, we selected from the data used to build GLAD-M25 a subset of 453 seismic sources that illuminate the target region, within the magnitude range $5.5 \leq M_w \leq 7.2$. In Fig. 2 (*left*), we render their focal mechanisms in different colors depending on hypocenter depth, deep (>300 km) versus shallow and intermediate earthquakes (<300 km). Fig. 2 (*middle*) shows all stations that fall inside the domain of interest, 380 land (yellow triangles) and 117 ocean-bottom (green triangles) seismometers. The target region, bounded by a thick black dashed outline, corresponds to one "chunk" of the cubed-sphere computational domain (Ronchi et al. 1996; Komatitsch et al. 2000) upon which GLAD-M25 was built. Source-receiver distances within this area include the teleseismic, and the equivalent body-wave bottoming depths span the mantle, albeit inhomogeneously. Hence, at least in principle, future regional inversions could be designed to run entirely within a single cubed-sphere chunk, although extending the model domain beyond that size might be called for. All waveforms were on file in the database made available by Lei et al. (2020).

For the model inter-comparison, we cross-validated GLAD-M25 and SEMUCB-WM1 by selecting 10 events from the global centroid moment tensor (GCMT) catalog (Ekström et al. 2012), none of which were included in the construction of either model. Their source-receiver paths are shown in Fig. 2 (*right*). They were chosen based on their isolated timing (i.e., no aftershocks, no simultaneous events), waveform quality (high signal-to-noise ratio), and likely short half-duration source moment magnitude ($6.3 \leq M_w \leq 6.9$). We used the GCMT solution as input to calculate synthetic data in both models using SPECFEM3D_GLOBE (Komatitsch et al. 2000), within which GLAD-M25
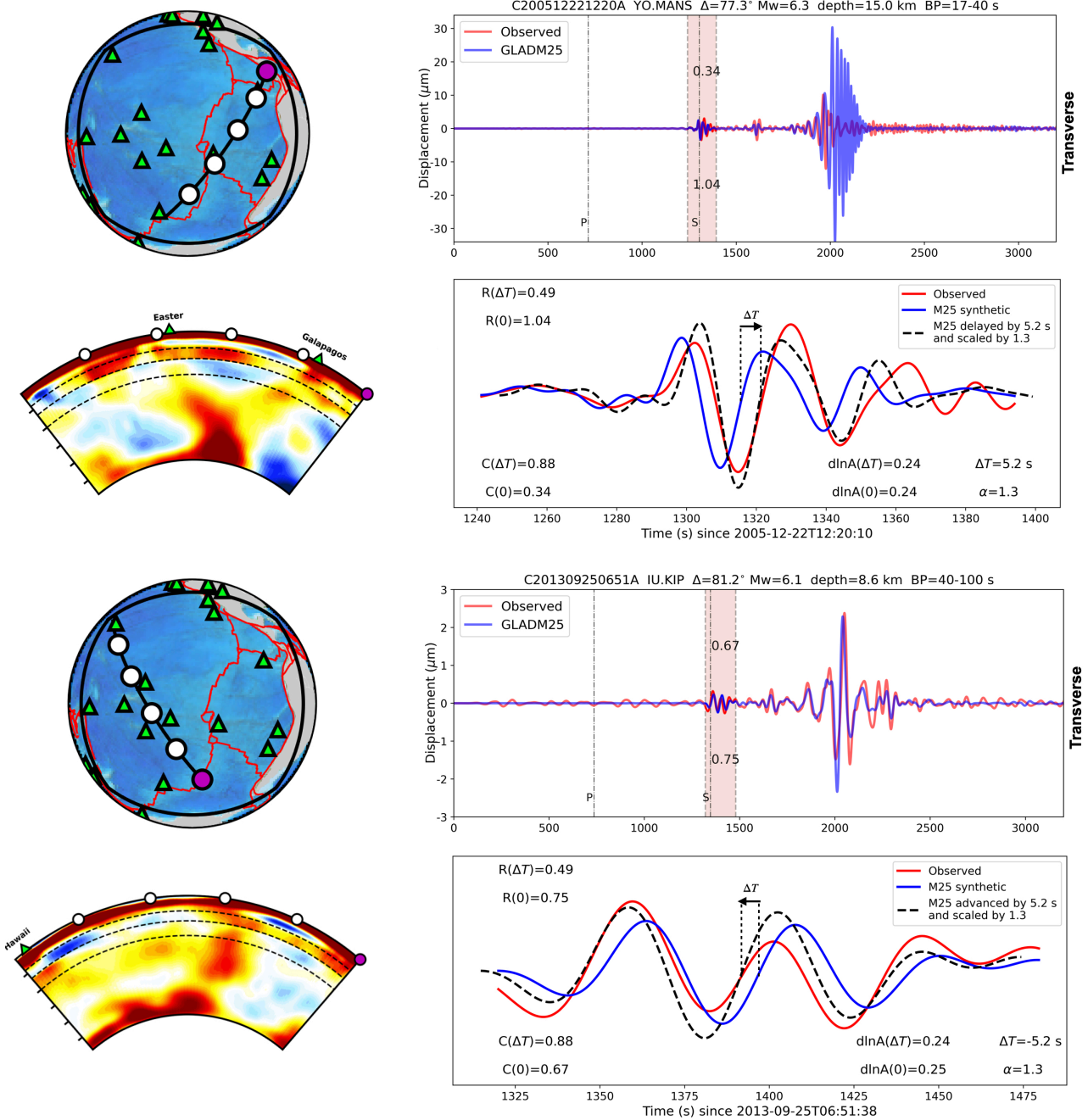
Figure 3. Cross-sections, seismograms, and waveform misfit metrics for body waves in two period bands, 17–40 s (*top set*), and 40–100 s (*bottom*). Each four-panel set presents a map view with the great-circle ray path connecting the earthquake source to the receiver (*top left*), a cross-section from East to West through model GLAD-M25 (*bottom left*) with the same color scale as in Fig. 1, and the subfigures (*right*) show a whole seismogram (*top*) and a zoom on the windowed shear (*S*) wave (*bottom*). Observed seismograms are red, the predictions, computed using SPECFEM3D_GLOBE in GLAD-M25, in blue. Numbers in the shaded portions are $R(0)$, below the trace, and $C(0)$, above it. In the zoomed-in sections, the synthetic seismograms are also shown, as dashed black lines, after shifting by the signed amount of the travel-time anomaly measurement, ΔT, and scaled by the factor $\alpha = \exp[\mathrm{dln}A(\Delta T)]$, which brings them into maximal alignment, as measured by the value of the cross-correlation coefficient, $C(\Delta T)$. In the top set, corresponding to station MANS in Costa Rica, the travel-time anomaly is positive, $\Delta T = +5.2$ s, indicating that the synthetic arrives earlier than the observed waveform (i.e., model GLAD-M25 is too fast). The scaled synthetic is delayed to align with the observations. In the bottom seismograms, recorded at station KIP, Hawaii, the anomaly is negative, $\Delta T = -5.2$ s, signifying a measurement in which the synthetic is late (i.e., the model too slow). The scaled synthetic is advanced into alignment, as shown.

was developed. While SEMUCB-WM1 itself was developed using CSEM by Capdeville et al. (2003), the model was incorporated into SPECFEM3D_GLOBE version 7.1 by Clouzet et al. (2018), with its three-dimensional crust expressed on the polynomial node grid, honoring lateral variations of the Moho, and benchmarked against CSEM. As to the moment tensors, the GLAD-M25 construction comprised an initial adjustment of source parameters as part of the inversion procedure, whereas SEMUCB-WM1 did not. While some of these procedural
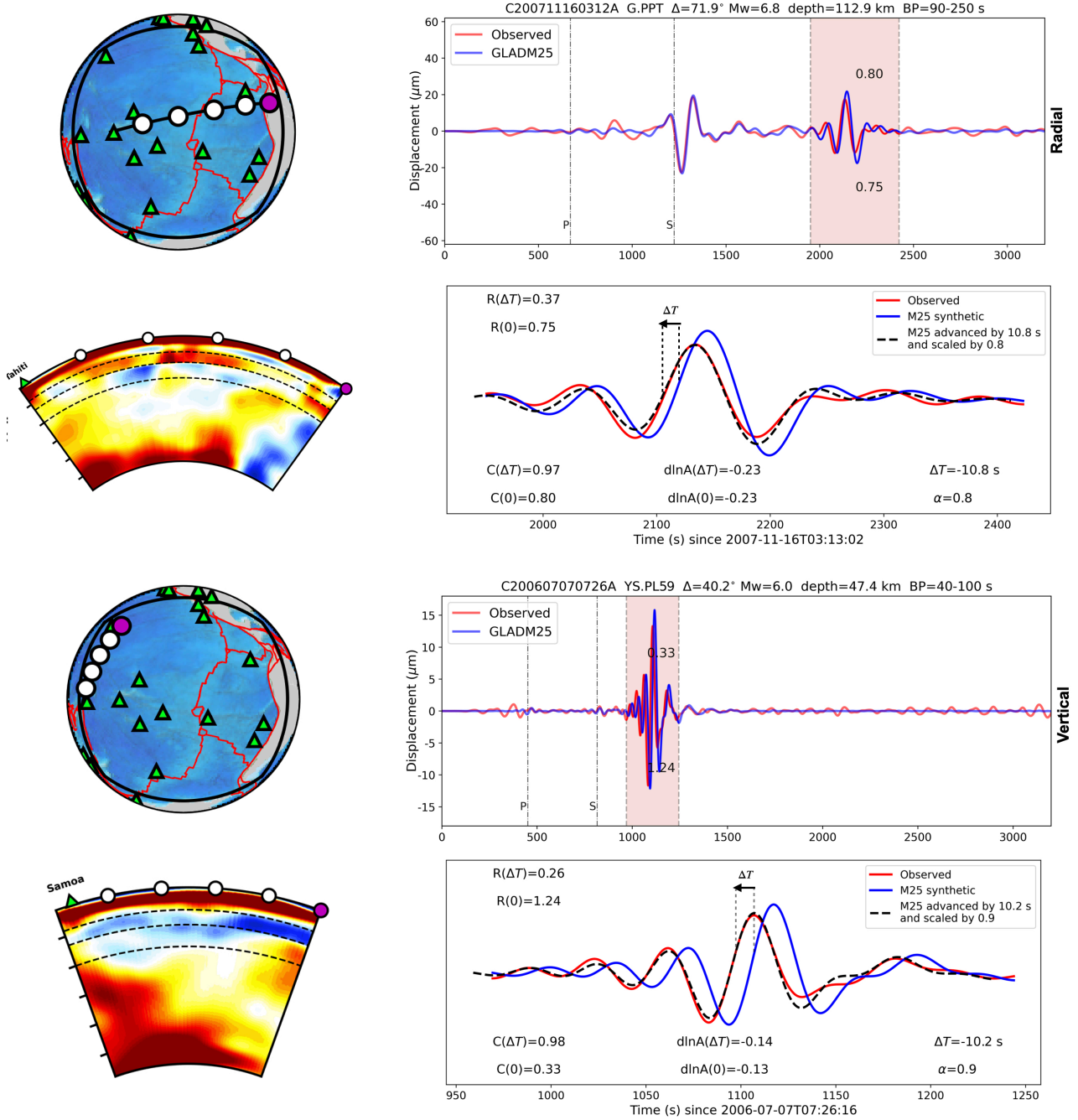
Figure 4. Cross-sections, seismograms, and waveform misfit metrics for surface waves in period bands 90–250 s (*top set*) and 40–100 s (*bottom*). Layout, labeling and color schemes are identical to Fig. 3, with observed seismograms in red, GLAD-M25 synthetics computed using SPECFEM3D_GLOBE in blue, and the dashed black traces showing the phase-and-amplitude corrected synthetic that is maximally aligned with the observations. Note that Fig. 3 showed two transverse-component seismograms, whereas here, we show one radial-component and one vertical-component case, as indicated by the labels to the right of the top panels of every set. The top seismograms are for a long oceanic path that is recorded on island station PPT (in Papeete, Tahiti). The bottom seismograms are for a shorter oceanic path recorded by ocean-bottom seismometer PL59 from the PLUME deployment near Hawaii (Laske et al. 2009). In both cases, the relevant wavespeeds in model GLAD-M25 are too slow for the trajectory. The synthetics need to be scaled, and advanced by $\Delta T = -10.8$ s and $\Delta T = -10.2$ s, respectively, to bring them into maximal alignment with the observations, as measured by the cross-correlation metric.

discrepancies may creep into individual waveform comparisons (see, e.g., Valentine & Woodhouse 2010), they are unlikely to show up in the statistical aggregates that we present. Moment-tensor adjustments due to three-dimensional wavespeed heterogeneity are typically small (Sawade et al. 2022). Furthermore, we are unable to make any model adjustments as part of our data-space validation with independent source data sets. Hence, we leave the GCMT solutions unchanged. A final note concerns the shear-to-compressional (*S*-to-*P*) wave speed scaling employed by SEMUCB-WM1. As in its original construction, we used the relationships proposed by Montagner & Anderson (1989), though it must be appreciated that the real mantle may be more complex (Koelemeijer et al. 2016; Moulik & Ekström 2016).

Many waveform misfit metrics are in use (Yuan et al. 2019). Here, the travel-time anomaly ΔT is the time lag that maximizes the normalized cross-correlation $C(\tau)$ between the observed, $d(t)$, and the synthetic, $s(t)$, seismograms in a window of length T starting at t_0,

$$\Delta T = \arg\max_{\tau}\{C(\tau)\}, \tag{1}$$

$$C(\tau) = \left(\int_{t_0}^{t_0+T} \left[d(t) - \bar{d} \right] \left[s(t-\tau) - \bar{s} \right] \mathrm{d}t \right) \Big/ \left(\int_{t_0}^{t_0+T} \left[d(t) - \bar{d} \right]^2 \mathrm{d}t \int_{t_0}^{t_0+T} \left[s(t-\tau) - \bar{s} \right]^2 \mathrm{d}t \right)^{1/2}, \tag{2}$$

with $\bar{d}$ and $\bar{s}$ the means of the data and the synthetics over the corresponding time interval. With this normalization, $C(\Delta T)$ is the cross-correlation coefficient between the overlapping segments of the observed and synthetic time series after shifting by ΔT. Without shifting, $C(0)$ is a measure of the data fit in the relevant tomographic model at the current iteration.

If we forgo the indices t_0 and T, and label the discretized shifted time series d_i and s_i^{τ} for paths i, a concise notation is

$$C(\tau) = \left(\sum_i \left[d_i - \bar{d} \right] \left[s_i^{\tau} - \bar{s} \right] \right) \Big/ \left(\sum_i \left[d_i - \bar{d} \right]^2 \sum_i \left[s_i^{\tau} - \bar{s} \right]^2 \right)^{1/2}. \tag{3}$$

An alternative approach to measuring the fit between the predicted and observed seismograms is to compute the relative root-mean squared (rms) waveform difference (see also Ritsema et al. 2002),

$$R(\tau) = \left(\sum_i \left[d_i - s_i^{\tau} \right]^2 \Big/ \sum_i \left[d_i - \bar{d} \right]^2 \right)^{1/2}. \tag{4}$$

A third metric is the amplitude anomaly between prediction and observation (Dahlen & Baig 2002; Maggi et al. 2009),

$$\mathrm{dln}A(\tau) = \frac{1}{2} \ln \left(\sum_i \left[d_i - \bar{d} \right]^2 \Big/ \sum_i \left[s_i^{\tau} - \bar{s} \right]^2 \right). \tag{5}$$

The resulting best-fit scaling factor is given by $\alpha = \exp[\mathrm{dln}A(\Delta T)]$.

For each window, metrics are computed at the time-shift that optimizes the cross-correlation, $\tau = \Delta T$, and at the current state of the model, $\tau = 0$. A negative travel-time anomaly, $\Delta T < 0$, signifies a late predicted arrival, i.e., a wavespeed model that is too slow over the average trajectory. A positive travel-time anomaly, $\Delta T > 0$, indicates an early predicted arrival, i.e., a model that is relatively too fast. Large relative travel-time shifts ΔT, and positive cross-correlation values $C(\Delta T)$ that are high relative to $C(0)$, indicate that the current model retains the potential for improvement. In that case, in principle, subsequent model iterations (e.g., regionally focused ones, Zhu et al. 2012; Cui et al. 2023) should help improve the synthetics to approximate the observations more closely.

Examples of data, measurements, and metrics across a range of long and short paths, land-based and ocean-bottom seismic stations, are shown in Figs 3 and 4. Fig. 3 focuses on seismic body waves, and Fig. 4 highlights surface waves. All three-component waveforms were filtered into three period bands, 17–40 s, 40–100 s, and 90–250 s. The body waves were partitioned into the period ranges 17–40 s and 40–100 s, whereas the surface waves were split into the categories 40–100 s and 90–250 s. In addition to listing the cross-correlations $C(0)$ and $C(\Delta T)$, the amplitude measurements $\mathrm{dln}A(0)$ and $\mathrm{dln}A(\Delta T)$, both figures also quote the relative root-mean-squared (rms) waveform differences, $R(0)$ and $R(\Delta T)$.

GLAD-M25 relies on hundreds of thousands of seismogram segments and some seismic traces have multiple windows that were measured, as is the case for the first waveform shown in Fig. 3. The shaded areas list the current rms, $R(0)$, below the trace, and the current cross-correlation, $C(0)$, above it. Observed seismograms are in red, and the synthetics, computed in GLAD-M25, are in blue. For the zoomed-in portions, the aligned signal, phase and amplitude-corrected by advancing or delaying it by ΔT and scaled by α, is shown dashed in black. It is apparent that some waveforms are not completely optimized, yet can be made to fit well after future adjustments. Such is the case for body and surface wave windows, for land stations and also for ocean-bottom-seismometer data.

3 RESULTS

Here, we present our analysis of the travel-time anomalies that survive in both global tomographic models. For model GLAD-M25, we compare the distributions of global data fits with those of the regional subset in the Pacific domain, for both body and surface waves. We discuss their geographic distribution, and we compare the difference between paths sampled by land-based and ocean-bottom seismometers. Second, we compare regional data fit metrics for the new, independent, data set, under both models GLAD-M25 and SEMUCB-WM1.

3.1 Global to Regional: Data-space intra-comparison of model GLAD-M25

To understand how well models explain data beneath the Pacific Ocean, we examine a regionally targeted subset of the global data set that was used in building global model GLAD-M25. Figs 5 and 6 summarize the results of our statistical analysis. We present histograms of normalized travel-time anomalies, $\Delta T/T$, in per cent. To compute these we divided the measured travel-time anomalies by the time of the midpoint of the measurement window, measured relative to the earthquake origin time. To first order, these metrics approximate the relative velocity anomaly, $\Delta c/c$, averaged over the path sampled by the specific phases, with c equal to the P-, S-, or surface-wave phase speed.
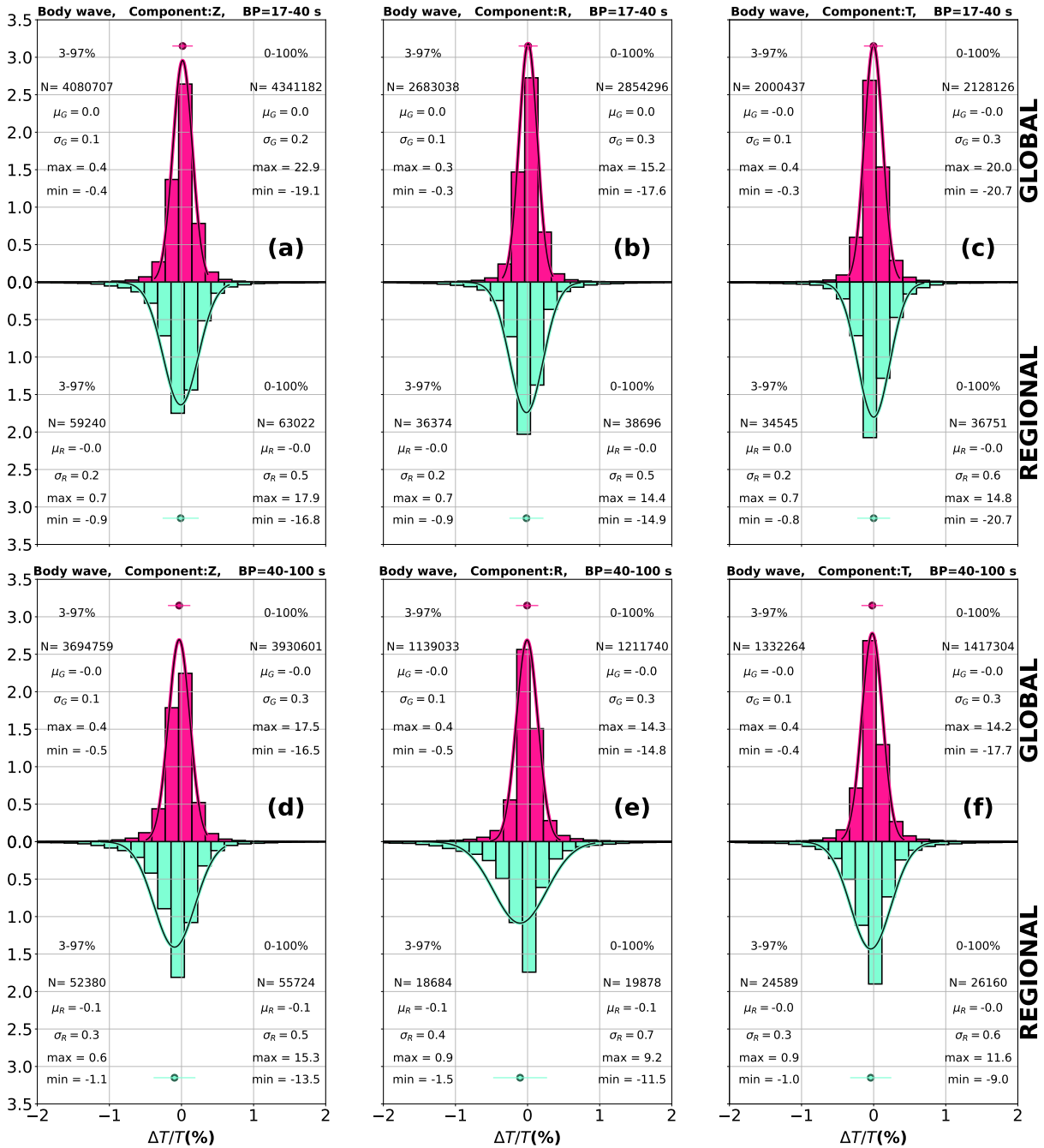
Figure 5. Distribution of normalized body-wave travel-time anomalies that persist in adjoint-based seismic tomography model GLAD-M25, for the Pacific target region and as compared to the entire globe. Histograms are shown for body waves across three seismogram components (vertical Z, radial R, and transverse T) and in two period bands, 17–40 s (*top row*, a–c) and 40–100 s (*bottom row*, d–f). Histograms of all global measurements are shaded fuchsia, those of the regional event-station subsets of Fig. 2 (*left* and *middle*) are in aquamarine, shown upside down. Means and plus-minus one standard deviation ranges hover over the bar graphs. Normal distributions are superimposed as solid curves. Values listed on the left side of every panel are computed after removing outliers not within the 3rd–97th percentile range, whereas the values on the right were computed using all of the data for each category. All global averages are indistinguishable from zero, and all global standard deviations are 0.1 s, suggesting unbiased model residuals and globally extremely tight data fits. Regional distributions are only slightly offset from zero, but their standard deviations are two to three times larger than the global values. The regional distributions also have heavier tails, suggesting that a sizable fraction of the data remains to be fully explained by the wavespeed model in the target region.

There are twelve different categories in all: two dominant wave types (body and surface, as indicated in the title of each panel), three components (radial R, transverse T, and vertical V, as listed) and three period bands (17–40 s and 40–100 s for the body waves, 40–100 s and 90–250 s for the surface waves). The number of measurement windows represented by histograms in each category, N, is reported in the annotation of each panel. The number of bins, n, in each histogram follows Sturges' rule, $n = 1 + \log_2(N)$, where N is the number of data. For the tabulated values shown inside the panels of Figs 5 and 6 we report both trimmed (between the 3% and 97% percentiles) and untrimmed (0% to 100%) statistics, as listed at the top of each summary table. Gaussian probability density functions with means and
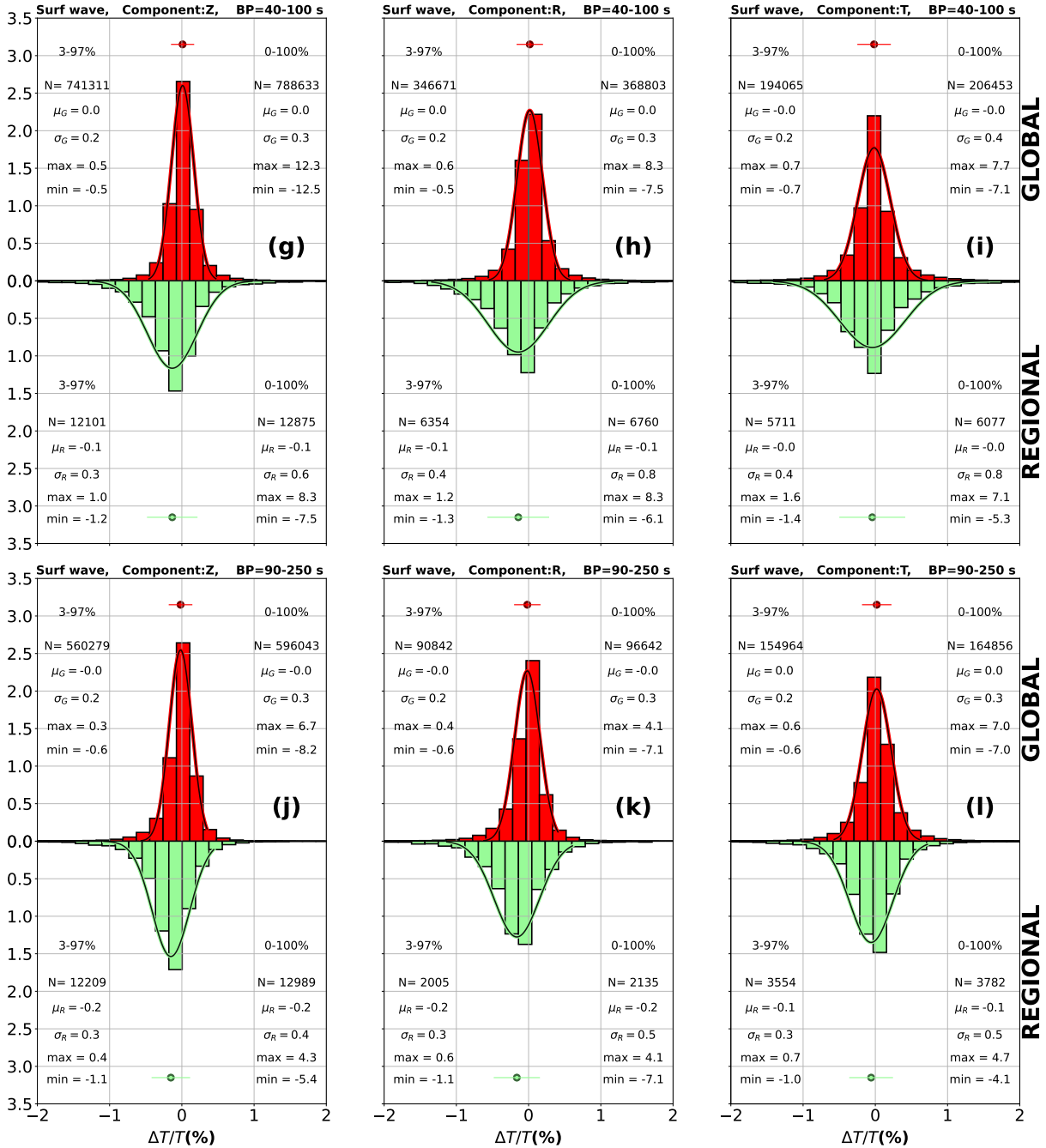
Figure 6. Distribution of normalized surface-wave travel-time anomalies persisting in model GLAD-M25, for the Pacific target region as compared to the whole globe. Histograms are for surface waves across three seismogram components (vertical Z, radial R, transverse T) in period bands 40–100 s (*top row*, g–i) and 90–250 s (*bottom row*, j–l). Layout and labeling are exactly as in Fig. 5. Again, the global distribution is always centered on zero within each category. In contrast, the regional distributions are shifted slightly towards more negative values, showing increased standard deviations and stronger contributions from the tails. For both Figs 5 and 6 all predicted waveforms were computed during the construction of GLAD-M25 using SPECFEM3D_GLOBE by Lei et al. (2020).

variances calculated after trimming are superimposed. In both Figs 5 and 6, histograms for the global data set that was presented and discussed by Lei et al. (2020) are shown right side up, whereas for the regional subsets pertaining to the events and land and ocean stations shown in Fig. 2 (*left* and *middle*), the histograms are flipped upside down.

The body-wave travel-time anomaly distributions shown in Fig. 5 are broader in the regional domain, i.e., for paths in the Pacific, than for all paths globally, with more windows displaying $|\Delta T/T| \geq 0.5\%$ regionally. Comparing the global and regional distributions for body waves between 17–40 s, Figs 5a–c show that the regional standard deviations are twice those of the global values. As frequency decreases and we consider long-period body waves between 40–100 s period, in Figs 5d–f, the trimmed regional standard deviations increase and the differences with their global equivalents grow. Observations made for surface waves are revealed by the distributions given in Fig. 6, for the wave packets filtered between periods 40–100 s, Fig. 6g–i, and between 90–250 s, Fig. 6j–l, which are sensitive down to the upper mantle and to the transition zone, respectively. Again the global remaining travel-time anomalies fit relatively Gaussian distributions centered at zero.
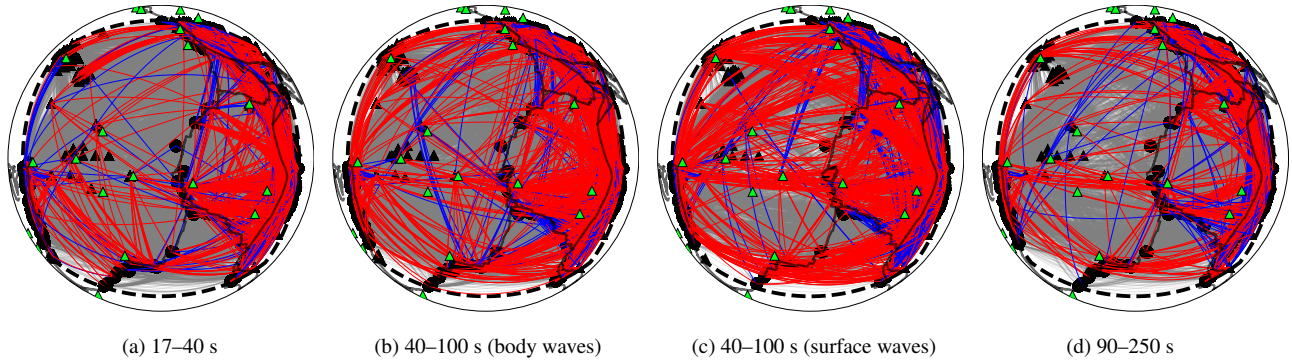
(a) 17–40 s	(b) 40–100 s (body waves)	(c) 40–100 s (surface waves)	(d) 90–250 s

Figure 7. Geographic distribution of relative travel-time velocity anomalies in GLAD-M25 for all paths sampling the target region, dashed in black, broken down by wave type and frequency band, across all seismogram components, and averaged over all analysis windows. We focus on the tails of the regional distributions shown in Figs 5–6. All paths with a good misfit between the observed and predicted waveforms (i.e., $-0.5\% < \overline{\Delta T/T} < +0.5\%$) are plotted in gray first. These are overlain by all other paths (i.e., $|\overline{\Delta T/T}| \geq 0.5\%$) sorted by absolute value. Red paths with negative anomalies ($\overline{\Delta T/T} < -0.5\%$) correspond to corridors where the velocity model is too slow. Blue paths with positive anomalies ($\overline{\Delta T/T} > +0.5\%$) signify that the model is too fast. Events and stations are shown by black circles and triangles, respectively, and hot spots are shown as green triangles. Plate boundaries are overlain in black lines.

On the other hand, the distributions of the regional travel-time anomalies are slightly shifted from the global distributions, and they appear flatter, with larger standard deviations and more outliers in the tails. The negative mean travel-time anomalies in the target region are most pronounced in the 90–250 s surface-wave band, suggesting that the model in and above the transition zone is overall slower than the real Earth. While crustal effects could play a role, our interpretation of these results is that significant exploitable mantle structure remains in the current data set, indicative of structure underneath the target region that is relatively more poorly resolved than for the globe as a whole.

To understand the geographic distribution of the regional residuals remaining in GLAD-M25, we average the relative travel-time anomalies summarized in Figs. 5–6 over all analysis windows and all components, which results in path average values, $\overline{\Delta T/T}$, for each data category. In Fig. 7, arranged as before by frequency band and wave type, we plot those paths in order of absolute value: in grey where the model predicts the path averages well, $|\overline{\Delta T/T}| < 0.5\%$, red where they are negative ($\overline{\Delta T/T} < -0.5\%$, and thus model too slow) and blue where they are positive ($\overline{\Delta T/T} > 0.5\%$, and hence the model too fast). In every category, the relative travel-time anomalies are small for over 75% of paths analyzed, indicating that GLAD-M25 represents average seismic velocities well for those paths. Across the categories, the 40–100 s period band has the highest fraction of strongly anomalous paths, $|\overline{\Delta T/T}| > 0.5\%$. For all categories, corridors where GLAD-M25 is too slow outnumber those where the model is too fast. In the 17–40 s band the negative (red) outliers comprise 8% of the total, against 5% for the positive (blue) outliers. For the 40–100 s body wave category those numbers are 12% compared 4%, for the 40–100 s surface they are 15% versus 7%, and finally, for the 90–250 s, they are 11% to 3%. In our region of interest, the strongest residual path-average anomalies are more likely to correspond to model corridors that are too slow than too fast, especially in the eastern portion of our region, beneath the Nazca Plate. Where there is a higher proportion of anomalous paths (in the period band 40-100 s), their geographical distribution is more diffuse, also covering portions of the Antarctic and Cocos Plates.

To evaluate the contribution of ocean-bottom seismometers (OBS) to the Pacific portion of global seismic model GLAD-M25, Fig. 8 presents a comparison of the travel-time anomaly distributions within the target region for land-based and OBS stations, identified in Fig 2. Very few OBS measurements (fewer than 2% of the total available number of analysis windows, noting that FLEXWIN often selects multiple short segments per trace) were included in the model, either in the body-wave or surface-wave categories. No OBS measurements were made on the horizontal components in the target region, which are generally noisier (Webb & Crawford 2010; Bell et al. 2015; Janiszewski et al. 2022; Zhang & Olugboji 2023). The majority of the OBS measurements are in the 17–40 s body wave window, where the mean and standard deviation of the anomalies correspond well to the land-based observations. In the lower-frequency bands there are fewer OBS data (less than 1000 in all cases, and only ∼100 for the lowest frequency window). The smaller number of lower-frequency OBS data make it harder to draw conclusions about the possible differences in travel-time anomaly distributions. Given the limited contribution of OBS data to this model, incorporating more marine data, whether from stationary or mobile instrumentation (Nolet et al. 2019; Simon et al. 2022), may considerably improve the spatial distribution of the measurements and the tomographic model in this area.

3.2   GLAD-M25 vs SEMUCB-WM1: Data-space model inter-comparison

The data sets and methodology used to develop global models GLAD-M25 (Lei et al. 2020) and SEMUCB-WM1 (French & Romanowicz 2015) are distinct, and hence it is to be expected that the resolution of mantle structure differs between both models.

The cross-section comparisons shown in Fig. 1 made it clear that both models do reveal mantle plumes beneath certain hotspots such as Samoa and Pitcairn, with differences mostly affecting model amplitudes: for example, the low shear-velocity anomaly beneath Samoa is stronger in GLAD-M25 than in SEMUCB-WM1, whereas in SEMUCB-WM1 the anomaly amplitude beneath Pitcairn is stronger, sharper, and more continuous than in GLAD-M25, which has smaller low-velocity anomalies below the transition zone and above the lowermost mantle. The Large Low Shear-Velocity Province (Garnero et al. 2016) at the core-mantle boundary beneath Tahiti and the Marquesas Islands
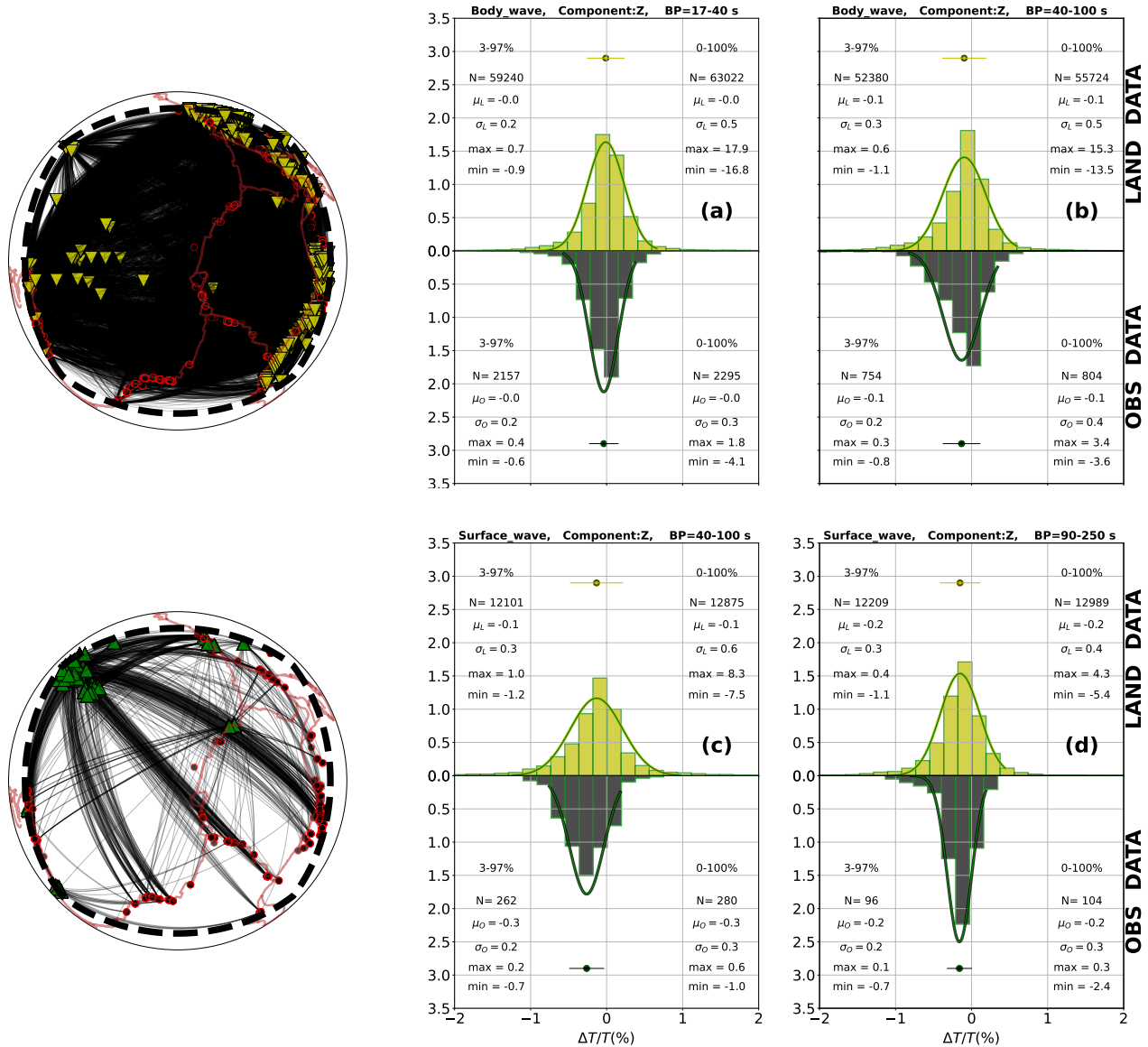
Figure 8. Distribution of normalized body-wave and surface-wave travel-time anomalies that persist in global tomography model GLAD-M25, comparing measurements made inside the Pacific target region at land-based stations (yellow histograms) versus ocean-bottom seismometers (dark grey upside-down histograms), for vertical-component recordings of body waves in the period bands 17–40 s and 40–100 s (a–b), and surface waves in the bands 90–250 s and 40–100 s (c–d). Note that comparatively very few OBS measurements were used in the construction of GLAD-M25, and none were made on the radial or transverse components. Annotations are as in Figs 5–6. The maps show ray paths between events (red circles), land (*top left*), and ocean-bottom (*bottom left*) seismometers (triangles), falling within the target region shown in Fig. 2. Note that the OBS ray paths are concentrated around four corridors which also stand out among the land-station ray paths. All waveform predictions were computed using SPECFEM3D_GLOBE during the construction of GLAD-M25.

appears to give rise to multiple plume conduits in both models, although the details of the morphology differ. In certain regions the lower-mantle structures are rather different in both models, for example, a low shear-velocity structure that appears in GLAD-M25 beneath the Easter Island, Galápagos and Juan Fernandez hotspots is very subdued in SEMUCB-WM1. Both models show different upper-mantle features across the Louisville, Easter, Galápagos, and Pitcairn hotspots. SEMUCB-WM1 exhibits a low-velocity structure beneath the Louisville hotspot that appears to rise from the mantle transition zone, which is weaker and offset in GLAD-M25.

Rather than comparing models through difference images or vote maps, via correlations, spectral content, or other statistics, as has been the tradition in the literature, we examine how the model differences might impact seismic waveforms themselves. To this end we produce an independent set of cross-validation data, and compute a second series of metrics as discussed in Sec. 2, suitable for exposing the differences between models through the data fits that they achieve. Fig. 2 (*right*) shows the path coverage achieved for this part of the analysis. Note that the sensitivities of finite-frequency seismic waves cover a volume more extensive than infinite-frequency ray paths (e.g., Hung et al. 2001).

Fig. 9 shows the details of how, for each event-station pair, we measured the cross-correlation between the observed and the predicted data, and the resulting travel-time anomaly, for synthetics newly computed in both models, on several time windows. For this particular event-station pair, SEMUCB-WM1 exhibits higher correlation values and lower travel-time anomalies for Rayleigh waves compared to
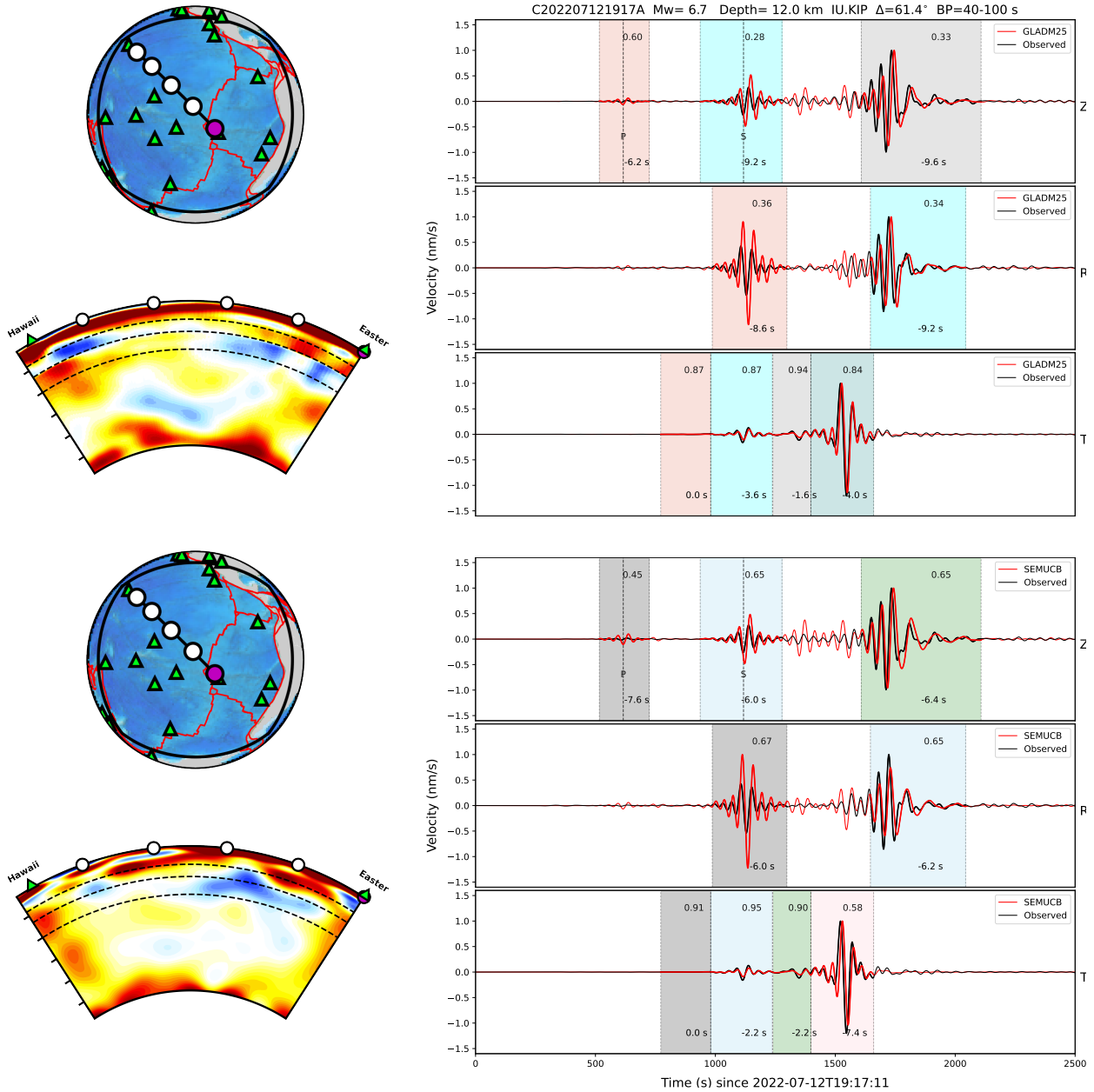
Figure 9. Comparison of waveforms predicted in GLAD-M25 *(top)* and SEMUCB-WM1 *(bottom)* with observed data (black) from event C202207121917A recorded at the central-Pacific seismic station KIP (Kipapa, Hawaii, USA). Comparison is performed in the same window, in the period range of 40–100 s, which includes both body and surface waves. The correlation between the observed and predicted data is shown at the top of each window, and the travel-time anomaly is at the bottom. The event used for our comparison was not used in building either model. Cross-sections through the tomographic models, using the same color scheme as Fig. 1, and great-circle paths are shown on the left.

GLAD-M25, while GLAD-M25 shows a better fit for Love waves. Although for this surface-wave path both models predict arrivals which are later than the observed data, SEMUCB-WM1 is faster than GLAD-M25 for Rayleigh waves, whereas GLAD-M25 is faster than SEMUCB-WM1 for Love waves. For body waves, any preference between SEMUCB-WM1 and GLAD-M25 is dependent on the specific choice of comparison window.

In the vein of the model intra-comparison shown in Figs 5–6, for the model inter-comparison we computed travel-time anomaly distributions, see Figs 10 and 11, for body and surface waves in the same period bands as before. For the body waves the residual anomalies in the band 17–40 s, Figs 10a–c, display histograms with heavy tails for both models, but especially for SEMUCB-WM1. This behavior is much less pronounced in the 40–100 s band, see Figs 10d–f. We interpret this difference between the outlier distribution measured in different period bands and the large absolute deviations in path-normalized travel-time anomalies as being due to unresolved short-wavelength structure in both models. Note, SEMUCB-WM1 was based on body-wave data with a minimum period of 32 s, compared to 17 s for GLAD-M25. The difference between the models is furthermore expressed in the surface waves, whose distributions are less centered and relatively shifted, especially in the period band of 90–250 s on all three components, see Figs 11j–l.
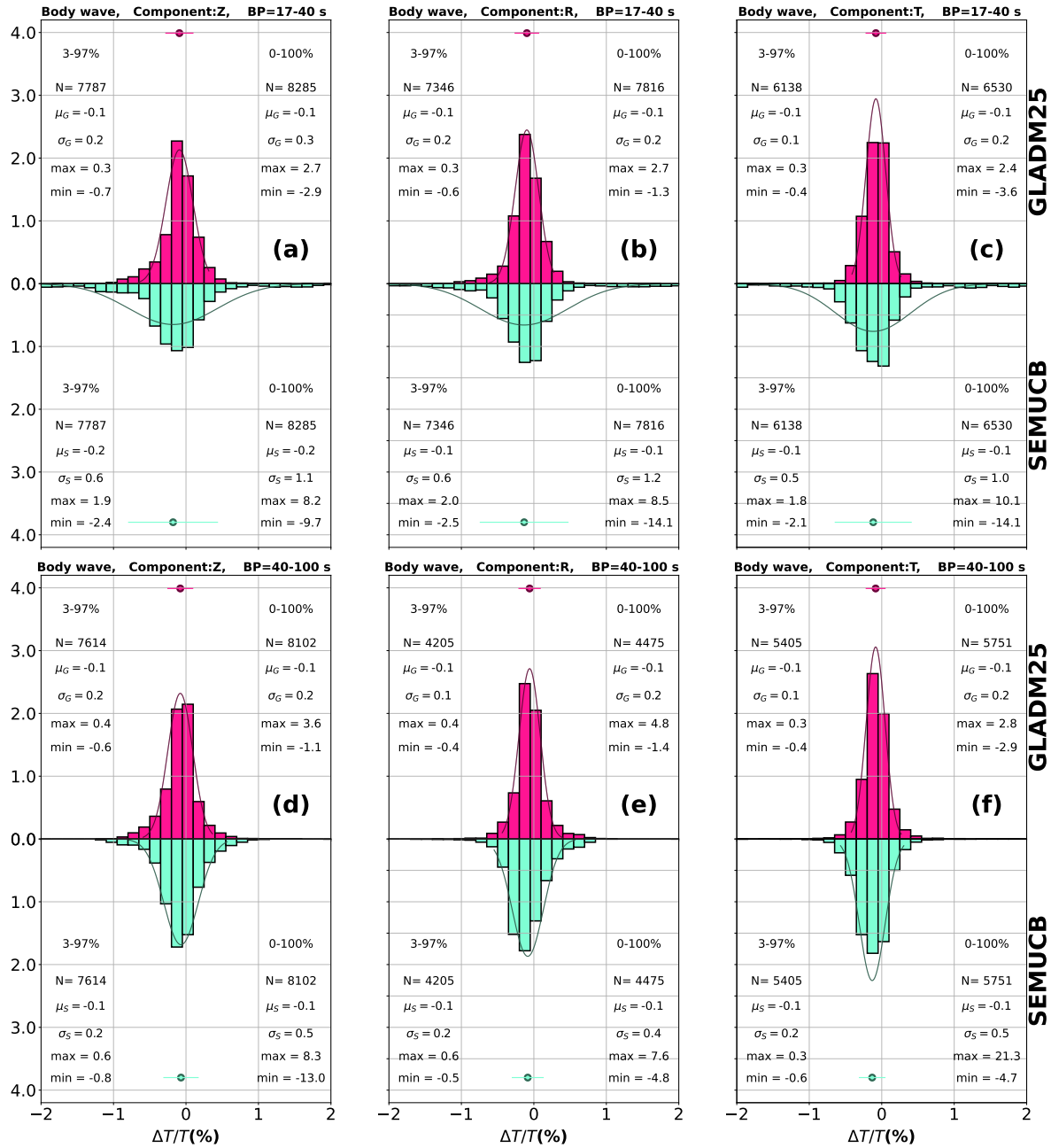
Figure 10. Normalized body-wave travel-time anomalies, measured on an independent data set covering the Pacific target region, that persist in GLAD-M25 (fuchsia histograms) and SEMUCB-WM1 (aquamarine, inverted). Body waves are separated into two period bands, 17–40 s (a–c) and 40–100 s (d–f). In the period range 17–40 s the travel-time anomaly distribution in SEMUCB-WM1 is less Gaussian, and standard deviations markedly larger than in GLAD-M25.

4 DISCUSSION

The two global seismic tomography models that we compared in the Pacific Ocean, GLAD-M25 and SEMUCB-WM1, show prominent low and high velocity anomalies in many similar locations throughout the mantle. Some of the differences are in amplitude, which might reflect variable levels of damping and other forms of regularization (Bozdağ & Trampert 2010), not to mention unavoidable biases due to choices of parameterization, especially with regards to anisotropy and attenuation. Important caveats are that while both models are parameterized to capture radial anisotropy, azimuthal anisotropy is wholly missing from the analysis, and the treatment or lack thereof of attenuation is another factor that may preclude truly "fair" comparisons between both models, and between data sets that may contain the unmodeled effects of anisotropy and anelasticity that are likely present in the "true" Earth (e.g., Karato 1993, 1998). All tomographic models are inevitably filtered versions of the Earth (Ritsema et al. 2007), hence all direct data comparisons, especially in regions that comprise geodynamically anomalous or geologically unique provinces (Ekström & Dziewoński 1998), are impacted by the specific modeling choices (Koelemeijer et al. 2018).

As shown in Fig. 1, the structure beneath the Pitcairn hotspot appears more continuous and better defined in SEMUCB-WM1 than in GLAD-M25. Beneath Hawaii, the SEMUCB-WM1 model tends to capture a weak low-velocity conduit, unlike GLAD-M25, where fast
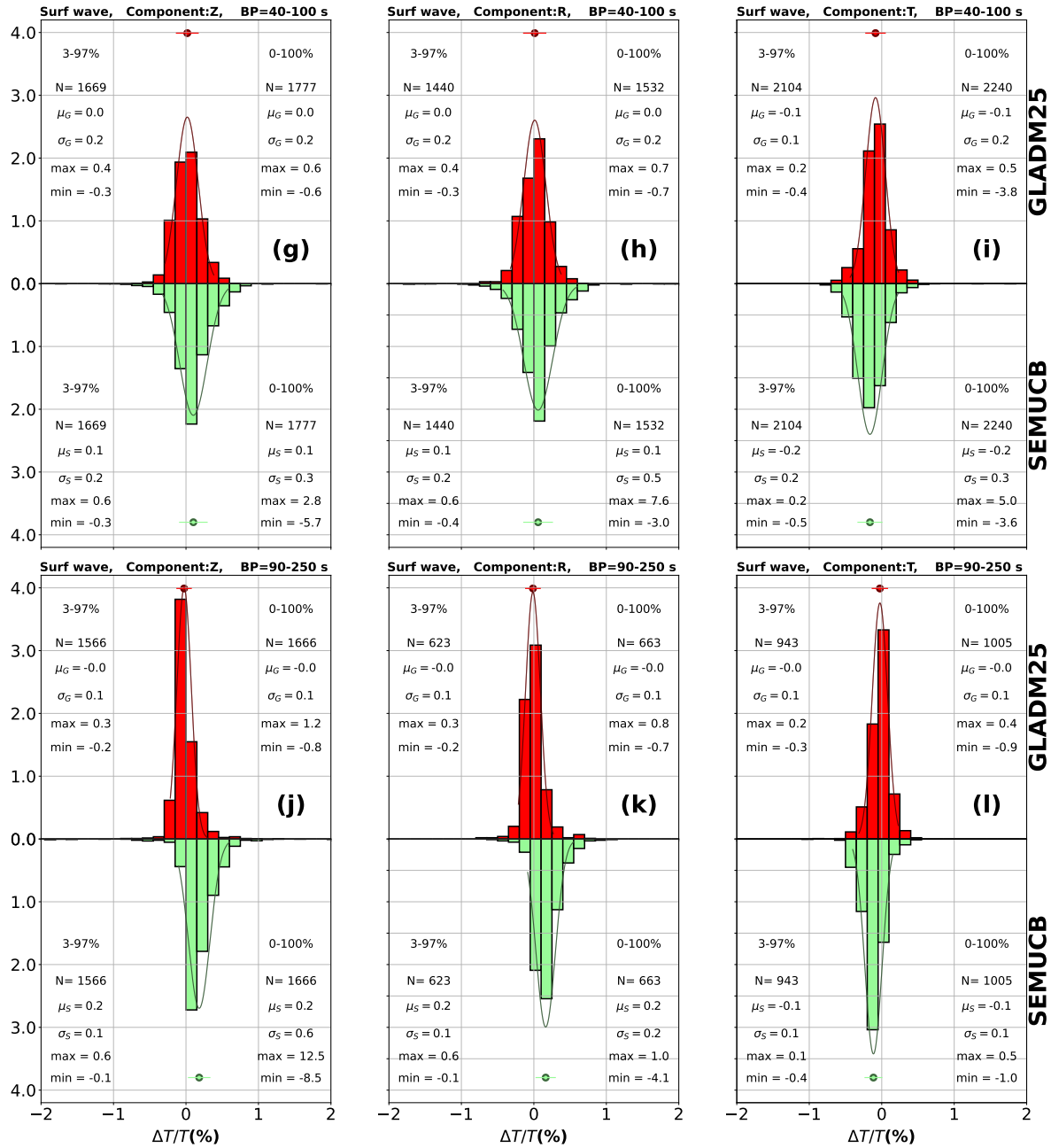
Figure 11. Normalized surface-wave travel-time anomalies, made on an independent data set within the Pacific target region, comparing GLAD-M25 to SEMUCB-WM1, laid out as for the body waves shown in Fig. 10, but now for surface waves, divided in two-period bands, 90–250 s (g-i) and 40–100 s (j–l).

material is present in the transition zone. A shear low-velocity structure observed beneath Samoa in both models is more pronounced in GLAD-M25 than in SEMUCB-WM1. Most significant are the model discrepancies in the lower mantle, e.g., beneath the Easter, Galápagos, and Juan Fernandez hotspots. Without explicit, specific, and targeted testing, e.g., via point-spread function or linear resolution analysis with synthetic anomalies (French & Romanowicz 2015; Lei et al. 2020) or by other means (e.g. Fichtner & Trampert 2011; Liu et al. 2022), we are neither able to ascertain if these differences are due to a lack of resolution, nor decide which of either model represents the true Earth.

In the data space, using our independent data set, both global models exhibit significant discrepancy at the longest (90–250 s) and shortest (17–40 s) periods. GLAD-M25 is delayed at long periods, and SEMUCB-WM1 shows heavy-tailed departures from the Gaussian distribution at short periods. It is likely that the lower mantle is not well resolved due to an unconstrained upper mantle. A two-step regional inversion, which involves constraining the upper mantle model with surface waves followed by adding overtones and body waves to access the mantle transition zone and lower mantle (e.g., Wamba et al. 2021), may be an efficient method for gaining insight into possible plume structure under certain hotspots, in particular, to ascertain their geometry as either vertically upwelling or ponding as in the Indian Ocean (Wamba et al. 2023; Tsekhmistrenko et al. 2021).

The present configuration of ray paths of OBS data incorporated into GLAD-M25 as shown by the path coverage plots in Fig. 8, largely samples the same corridors as the land-based stations, illustrating that additional oceanic data are especially desirable and should be collected

in the S–SW portion of the target region. As recommended elsewhere in the Pacific (Maguire et al. 2016), a dedicated OBS network could meaningfully improve both path density as a whole and the availability of crossing paths, vital to improving model resolution and reducing model uncertainty (Simons et al. 2002; Rawlinson et al. 2014; Ruan et al. 2019; Latallerie et al. 2022). There is scope for continued iteration with a focus on fitting data (from an expanded set of measurements) on and around the Pacific Superswell, either as a regional inverse problem (Cui et al. 2023) or as part of a whole new generation of global models. The former might need to be strictly regionally focused by confining both sources and receivers inside a target domain (ideally a single cubed-sphere chunk), or require special considerations to avoid contamination from unmodeled structure outside (Clouzet et al. 2018; Masson & Romanowicz 2017; Monteiller et al. 2020), whereas the latter might run into convergence issues and speed limitations. An expanded set of data may encompass additional seismic phases, including those arriving as major arc body waves, or targeting specific areas of the mantle (e.g. Cui et al. 2024), selecting smaller events to target specific geographic areas or depths, or advocating for and making use of new seismic stations.

Metrics relating observations to data predicted via spectral-element modeling in both models made on an independent data set indicate a mixture of relatively good and relatively poor fits throughout the various time and phase windows analyzed, as shown in the example of Fig. 9. On the whole, travel-time anomalies and correlation coefficients between synthetic and observed data windows do still exhibit relatively low and high values, respectively, for both models. The similarity between both models is greatest in the period band of 40–100 s for both body and surface waves. The discrepancy observed on long-period surface waves, in the period range 90–250 s, may motivate the construction of a regional upper-mantle and transition-zone model for the South Pacific.

Travel-time anomalies in the independent data set are larger than in the data used for the construction of GLAD-M25. The comparison of our regional data-space results with assessment tests performed on "held-back" data sets used during the construction of both global models GLAD-M25 and SEMUCB-WM1 (Lei et al. 2020; French & Romanowicz 2014), suggests the held-back sets are better fit in terms of their average travel-time anomalies, with lower residual standard deviations. This reinforces our interpretation that global models require probing and evaluation in specific geographic regions, as this allows us to focus on seismic ray paths that cross the target region, thereby sampling the relevant geological structures of most interest. It is precisely those areas of great geodynamical importance, i.e., in the plume-rich region underlying the Pacific Superswell (McNutt & Fischer 1987; McNutt & Judge 1990; McNutt 1998), that have had very limited passive seismic exploration. The ORCA project (Eilon et al. 2021) is a welcome recent exception, and valuable future deployments are planned as part of PacificArray (Kawakatsu et al. 2016; Isse et al. 2024). These portable ocean-bottom seismometry experiments may need to be augmented by non-traditional instrumentation, e.g., mobile marine sensors (Mᴇʀᴍᴀɪᴅ, Simon et al. 2022; Pipatprathanporn & Simons 2024).

5 CONCLUSIONS

Despite carefully designed weighting schemes to balance the relative geographic contributions of different data sets to tomographic inversions for global models (e.g., Ruan et al. 2019; Cui et al. 2023), regional portions of the globe may remain relatively under-resolved compared to the global average (a problem not confined to seismology, nor to this planet, see Plattner & Simons 2015). Global models GLAD-M25 (Lei et al. 2020) and SEMUCB-WM1 (French & Romanowicz 2015), obtained independently, have been very well received in the geophysical literature, and they have proved useful in the interpretation of other signals of deep Earth processes, such as those provided by geochemical analyses (Williams et al. 2019).

In this paper we first performed a regional assessment of the quality of GLAD-M25 in a Pacific target region centered on Polynesia, in order to ascertain its resolution of mantle structure and the potential for improvement by conducting subsequent regionally-focused model iterations and the addition of new data, especially those sampling oceanic paths measured at ocean-bottom stations or floating sensors available from past or future deployments. We studied the distribution of travel-time anomalies over a regionally selective subset of the data, obtained by the spectral-element method, as compared to the global data set that was used in constructing the model. The relatively significant discrepancy that still exists between the observed and predicted waveforms supports our hypothesis that it is likely that unresolved structure persists in the region containing several hotspots in Polynesia and surrounding areas. The travel-time anomaly distribution retains larger values in the target region than over the entire globe. Numerous waveforms recorded by seismic stations around Polynesia still show significant shifts when compared with their synthetic predictions. Our data analysis furthermore highlights the rather minor contribution of ocean-bottom-seismometer data to the current model, hence the significant potential for data addition from existing deployments, in particular from the horizontal components, and from adding new networks, especially in the S–SW reaches of our target region.

In addition to the regional intra-comparison of GLAD-M25, we performed a model inter-comparison between GLAD-M25 and SEMUCB-WM1. Simply comparing models based on selected cross-sections and depth slices, i.e., in model space, as has been the norm in comparative tomography, cannot reveal the impact of differences on seismic waveforms. Here we cross-validated both models in data space, by analyzing the distribution of waveform fits newly calculated for an independent data set. Models GLAD-M25 and SEMUCB-WM1 show discrepancies at shorter periods, between 17–40 s, where the travel-time anomaly distribution in SEMUCB-WM1 shows biases that remain unexplained. At the longer periods, 90–250 s, Rayleigh waves predicted by SEMUCB-WM1 are faster than for GLAD-M25, but the opposite holds for Love waves, possibly due to different trade-offs between isotropic and radially anisotropic structure in the construction of these two models. While both models are generally compatible with each other, and with their own data sets, our independent analysis will motivate and inform the design of future studies conducting regional tomography targeting the Pacific region in efforts to image currently unresolved seismic velocity anomaly structure, especially underneath hotspots.

DATA AVAILABILITY

ACKNOWLEDGMENTS

REFERENCES

Austermann, J., Kaye, B. T. & Mitrovica, J. X., 2014. A statistical analysis of the correlation between large igneous provinces and lower mantle seismic structure, *Geophys. J. Int.*, **197**(1), 1–9, doi: 10.1093/gji/ggt500.

Bassin, C., Laske, G. & Masters, G., 2000. The current limits of resolution for surface wave tomography in North America, *Eos Trans. AGU*, **81**, F897.

Becker, T. W. & Boschi, L., 2002. A comparison of tomographic and geodynamic mantle models, *Geochem. Geophys. Geosys.*, **3**(1), 1003, doi: 10.1029/2001GC000168.

Becker, T. W., Kellogg, J. B., Ekström, G. & O'Connell, R. J., 2003. Comparison of azimuthal seismic anisotropy from surface waves and finite-strain from global mantle-circulation models, *Geophys. J. Int.*, **155**(2), 696–714, doi: 10.1046/j.1365–246X.2003.02085.x.

Bell, S. W., Forsyth, D. W. & Ruan, Y., 2015. Removing noise from the vertical component records of ocean-bottom seismometers: Results from year one of the Cascadia Initiative, *B. Seismol. Soc. Am.*, **105**(1), 300–313, doi: 10.1785/0120140054.

Benoit, M. H., Long, M. D. & King, S. D., 2013. Anomalously thin transition zone and apparently isotropic upper mantle beneath Bermuda: Evidence for upwelling, *Geochem. Geophys. Geosys.*, **14**(10), 4282–4291, doi: 10.1002/ggge.20277.

Bozdağ, E. & Trampert, J., 2010. Assessment of tomographic mantle models using spectral element seismograms, *Geophys. J. Int.*, **180**(3), 1187–1199, doi: 10.1111/j.1365–246X.2009.04468.x.

Bozdağ, E., Peter, D., Lefebvre, M., Komatitsch, D., Tromp, J., Hill, J., Podhorszki, N. & Pugmire, D., 2016. Global adjoint tomography: first-generation model, *Geophys. J. Int.*, **207**(3), 1739–1766, doi: 10.1093/gji/ggw356.

Burky, A., Irving, J. C. E. & Simons, F. J., 2023. The mantle transition zone beneath eastern North America: Receiver functions and tomographic velocity models, *Phys. Earth Planet. Inter.*, **340**, 107035, doi: 10.1016/j.pepi.2023.107035.

Capdeville, Y., Chaljub, E. & Montagner, J.-P., 2003. Coupling the spectral element method with a modal solution for elastic wave propagation in global earth models, *Geophys. J. Int.*, **152**(1), 34–67, doi: 10.1046/j.1365–246X.2003.01808.x.

Ciardelli, C., Bozdağ, E., Peter, D. & van der Lee, S., 2022. SphGLLTools: A toolbox for visualization of large seismic model files based on 3D spectral-element meshes, *Comput. Geosci.*, **159**, 105007, doi: 10.1016/j.cageo.2021.105007.

Clouzet, P., Masson, Y. & Romanowicz, B., 2018. Box tomography: first application to the imaging of upper-mantle shear velocity and radial anisotropy structure beneath the North American continent, *Geophys. J. Int.*, **213**(3), 1849–1875, doi: 10.1093/gji/ggy078.

Collins, J. A., Vernon, F. L., Orcutt, J. A., Stephen, R. A., Peal, K. R., Wooding, F. B., Spiess, F. N. & Hildebrand, J. A., 2001. Broadband seismology in the oceans: Lessons from the Ocean Seismic Network Pilot Experiment, *Geophys. Res. Lett.*, **28**(1), 49–52, doi: 10.1029/2000GL011638.

Cottaar, S. & Lekić, V., 2016. Morphology of seismically slow lower-mantle structures, *Geophys. J. Int.*, **207**(2), 1122–1136, doi: 10.1093/gji/ggw324.

Courtillot, V., Davaille, A., Besse, J. & Stock, J., 2003. Three distinct types of hotspots in the Earth's mantle, *Earth Planet. Sci. Lett.*, **205**(3–4), 295–308, doi: 10.1016/S0012–821X(02)01048–8.

Cui, C., Bachmann, E., Peter, D. B., Liu, Z. & Tromp, J., 2023. Source-encoded waveform inversion in the Northern Hemisphere, *Geophys. J. Int.*, **235**, 2305–2322, doi: 10.1093/gji/ggad363.

Cui, C., Lei, W., Liu, Q., Peter, D., Bozdağ, E., Tromp, J., Hill, J., Podhorszki, N. & Pugmire, D., 2024. GLAD-M35: a joint P and S global tomographic model with uncertainty quantification, *Geophys. J. Int.*, **239**(1), 478–502, doi: 10.1093/gji/ggae270.

Dahlen, F. A. & Baig, A., 2002. Fréchet kernels for body-wave amplitudes, *Geophys. J. Int.*, **150**, 440–466, doi: 10.1046/j.1365–246X.2002.01718.x.

Dannberg, J. & Sobolev, S. V., 2015. Low-buoyancy thermochemical plumes resolve controversy of classical mantle plume concept, *Nat. Commun.*, **6**(1), 6960, doi: 10.1038/ncomms7960.

Davaille, A., Carrez, P. & Cordier, P., 2018. fat plumes may reflect the complex rheology of the lower mantle, *Geophys. Res. Lett.*, **45**(3), 1349–1354, doi: 10.1002/2017GL076575.

Durek, J. J. & Ekström, G., 1996. A radial model of anelasticity consistent with long-period surface-wave attenuation, *B. Seismol. Soc. Am.*, **86**(1A), 144–158, doi: 10.1785/BSSA08601A0144.

Eilon, Z. C., Gaherty, J. B., Zhang, L., Russell, J., McPeak, S., Phillips, J., Forsyth, D. W. & Ekström, G., 2021. The Pacific OBS Research into Convecting Asthenosphere (ORCA) experiment, *Seismol. Res. Lett.*, **93**(1), 477–493, doi: 10.1785/0220210173.

Ekström, G. & Dziewoński, A. M., 1998. The unique anisotropy of the Pacific upper mantle, *Nature*, **394**(6689), 168–172, doi: 10.1038/28148.

Ekström, G., Nettles, M. & Dziewonski, A. M., 2012. The global CMT project 2004–2010: Centroid-moment tensors for 13,017 earthquakes, *Phys. Earth Planet. Inter.*, **200–201**, 1–9, doi: 10.1016/j.pepi.2012.04.002.

Faccenda, M. & VanderBeek, B. P., 2023. On constraining 3D seismic anisotropy in subduction, mid-ocean-ridge, and plume environments with teleseismic body wave data, *J. Geodyn.*, **158**, 102003, doi: 10.1016/j.jog.2023.102003.

Fichtner, A. & Trampert, J., 2011. Resolution analysis in full waveform inversion, *Geophys. J. Int.*, **187**(3), 1604–1624, doi: 10.1111/j.1365–246X.2011.05218.x.

Fouch, M. J., Fischer, K. M. & Wysession, M. E., 2001. Lowermost mantle anisotropy beneath the Pacific: Imaging the source of the Hawaiian plume, *Earth Planet. Sci. Lett.*, **190**(3–4), 167–180, doi: 10.1016/S0012–821X(01)00380–6.

Foulger, G. R., 2002. Plumes, or plate tectonic processes?, *Astron. Geoph.*, **43**(6), 6–19, doi: 10.1046/j.1468–4004.2002.43619.x.

Foulger, G. R., 2021, The plate theory for volcanism, in *Encyclopedia of Geology*, edited by D. Alderton & S. A. Elias, vol. 3, pp. 879–890, doi: 10.1016/B978–0–08–102908–4.00105–3, Academic Press, London, UK.

French, S., Lekic, V. & Romanowicz, B., 2013. Waveform tomography reveals channeled flow at the base of the oceanic asthenosphere, *Science*, **342**(6155), 227–230, doi: 10.1126/science.124151.

French, S. W. & Romanowicz, B., 2015. Broad plumes rooted at the base of the Earth's mantle beneath major hotspots, *Nature*, **525**, 95–99, doi: 10.1038/nature14876.

French, S. W. & Romanowicz, B. A., 2014. Whole-mantle radially anisotropic shear velocity structure from spectral-element waveform tomography, *Geophys. J. Int.*, **199**(3), 1303–1327, doi: 10.1093/gji/ggu334.

Fukao, Y., Widiyantoro, S. & Obayashi, M., 2001. Stagnant slabs in the upper and lower mantle transition region, *Rev. Geophys.*, **39**(3), 291–323, doi: 10.1029/1999RG000068.

Gaherty, J. B., 2001. Seismic evidence for hotspot-induced buoyant flow beneath the Reykjanes Ridge, *Science*, **293**(5535), 1645–1647, doi: 10.1126/science.106156.

Garnero, E. J., McNamara, A. K. & Shim, S.-H., 2016. Continent-sized anomalous zones with low seismic velocity at the base of Earth's mantle, *Nature Geosci.*, **9**(7), 481–489, doi: 10.1038/NGEO2733.

Grand, S. P., van der Hilst, R. D. & Widiyantoro, S., 1997. Global seismic tomography: A snapshot of convection in the Earth, *GSA Today*, **7**(4), 1–7.

Gülcher, A. J. P., , Golabek, G. J., Thielmann, M., Ballmer, M. D. & Tackley, P. J., 2022. narrow, fast, and "cool" mantle plumes caused by strain-weakening rheology in Earth's lower mantle, *Geochem. Geophys. Geosys.*, **23**(10), e2021GC010314, doi: 10.1029/2021GC010314.

Hansen, S. E., Graw, J. H., Kenyon, L. M., Nyblade, A. A., Wiens, D. A., Aster, R. C., Huerta, A. D., Anandakrishnan, S. & Wilson, T., 2014. Imaging the Antarctic mantle using adaptively parameterized P-wave tomography: Evidence for heterogeneous structure beneath West Antarctica, *Earth Planet. Sci. Lett.*, **408**, 66–78, doi: 10.1016/j.epsl.2014.09.043.

Hernlund, J. W. & Houser, C., 2008. On the statistical distribution of seismic velocities in Earth's deep mantle, *Earth Planet. Sci. Lett.*, **265**(3–4), 423–437, doi: 10.1016/j.epsl.2007.10.042.

Hung, S.-H., Dahlen, F. A. & Nolet, G., 2001. Wavefront healing: a banana-doughnut perspective, *Geophys. J. Int.*, **146**, 289–312, doi: 10.1046/j.1365–246x.2001.01466.x.

Isse, T., Kawakatsu, H., Lee, S.-M., Kuo, B.-Y. & Gaherty, J. B., 2024. Pacific Array: international collaboration for large-scale array experiment in the Pacific basin, *Geophys. Res. Abstr.*, pp. EGU24–4486, doi: 10.5194/egusphere–egu24–4486.

Janiszewski, H. A., Eilon, Z., Russell, J. B., Brunsvik, B., Gaherty, J. B., Mosher, S. G., Hawley, W. B. & Coats, S., 2022. Broad-band ocean bottom seismometer noise properties, *Geophys. J. Int.*, **233**(1), 297–315, doi: 10.1093/gji/ggac450.

Jordan, T. H., Puster, P., Glatzmaier, G. A. & Tackley, P. J., 1993. Comparisons between seismic Earth structures and mantle flow models based on radial correlation functions, *Science*, **261**(5127), 1427–1431.

Karato, S., 1993. Importance of anelasticity in the interpretation of seismic tomography, *Geophys. Res. Lett.*, **20**(15), 1623–1626, doi: 10.1029/93GL01767.

Karato, S.-I., 1998. Seismic anisotropy in the deep mantle, boundary layers and the geometry of mantle convection, *Pure Appl. Geophys.*, **151**, 565–587, doi: 10.1007/s000240050130.

Karato, S.-I., Jung, H., Katayama, I. & Skemer, P., 2008. Geodynamic significance of seismic anisotropy of the upper mantle: New insights from laboratory studies, *Annu. Rev. Earth Pl. Sc.*, **36**, 59–95, doi: 10.1146/annurev.earth.36.031207.124120.

Kawakatsu, H., Ekström, G., Evans, R., Forsyth, D., Gaherty, J., Kennett, B., Montagner, J.-P., & Utada, H., 2016. Pacific Array (Transportable Broadband Ocean Floor Array), *Geophys. Res. Abstr.*, **18**, EGU2016–2514.

King, S. D. & Adam, C., 2014. Hotspot swells revisited, *Phys. Earth Planet. Inter.*, **235**, 66–83, doi: 10.1016/j.pepi.2014.07.006.

Koelemeijer, P., Ritsema, J., Deuss, A. & van Heijst, H.-J., 2016. Sp12rts: a degree-12 model of shear-and compressional-wave velocity for Earth's mantle, *Geophys. J. Int.*, **204**(2), 1024–1039, doi: 10.1093/gji/ggv481.

Koelemeijer, P., Schuberth, B. S., Davies, D. R., Deuss, A. & Ritsema, J., 2018. Constraints on the presence of post-perovskite in Earth's lowermost mantle from tomographic-geodynamic model comparisons, *Earth Planet. Sci. Lett.*, **494**, 226–238, doi: 10.1016/j.epsl.2018.04.056.

Kohler, M. D., Hafner, K., Park, J., Irving, J. C. E., Caplan-Auerbach, J., Collins, J., Berger, J., Tréhu, A. M., Romanowicz, B. & Woodward, R. L., 2020. A plan for a long-term, automated, broadband seismic monitoring network on the global seafloor, *Seismol. Res. Lett.*, **91**(3), 1343–1355, doi: 10.1785/0220190123.

Komatitsch, D., Barnes, C. & Tromp, J., 2000. Wave propagation near a fluid-solid interface: A spectral-element approach, *Geophysics*, **65**(2), 623–631, doi: 10.1190/1.1444758.

Koppers, A. A. P., Becker, T. W., Jackson, M. G., Konrad, K., Müller, R. D., Romanowicz, B., Steinberger, B. & Whittaker, J. M., 2021. Mantle plumes and their role in earth processes, *Nat. Rev. Earth Env.*, **2**(6), 382–401, doi: 10.1038/s43017–021–00168–6.

Kustowski, B., Ekström, G. & Dziewoński, A. M., 2008. Anisotropic shear-wave velocity structure of the Earth's mantle: A global model, *J. Geophys. Res.*, **113**(B6), B06306, doi: 10.1029/2007JB005169.

Laske, G., Collins, J. A., Wolfe, C. J., Solomon, S. C., Detrick, R. S., Orcutt, J. A., Bercovici, D. & Hauri, E. H., 2009. Probing the Hawaiian hot spot with new broadband ocean bottom instruments, *Eos Trans. AGU*, **90**(41), 361–363, doi: 10.1029/2009EO410002.

Latallerie, F., Zaroli, C., Lambotte, S. & Maggi, A., 2022. Analysis of tomographic models using resolution and uncertainties: a surface wave example from the Pacific, *Geophys. J. Int.*, **230**(2), 893–907, doi: 10.1093/gji/ggac095.

Lei, W., Ruan, Y., Bozdağ, E., Peter, D., Lefebvre, M., Komatitsch, D., Tromp, J., Hill, J., Podhorszki, N. & Pugmire, D., 2020. Global adjoint tomography—

model GLAD-M25, *Geophys. J. Int.*, **223**(1), 1–21, doi: 10.1093/gji/ggaa253.

Lekić, V. & Romanowicz, B., 2011. Inferring upper-mantle structure by full waveform tomography with the spectral element method, *Geophys. J. Int.*, **185**(2), 799–831, doi: 10.1111/j.1365–246X.2011.04969.x.

Lekić, V., Cottaar, S., Dziewonski, A. & Romanowicz, B., 2012. Cluster analysis of global lower mantle tomography: A new class of structure and implications for chemical heterogeneity, *Earth Planet. Sci. Lett.*, **357–358**, 68–77, doi:10.1016/j.epsl.2012.09.014.

Li, C., van der Hilst, R. D., Engdahl, E. R. & Burdick, S., 2008. A new global model for *P* wave speed variations in Earth's mantle, *Geochem. Geophys. Geosys.*, **9**(5), Q05018, 10.1029/2007GC001806.

Li, X.-D. & Romanowicz, B., 1995. Comparison of global waveform inversions with and without considering cross-branch modal coupling, *Geophys. J. Int.*, **121**(3), 695–709, doi: 10.1111/j.1365–246X.1995.tb06432.x.

Liu, Q. & Gu, Y. J., 2012. Seismic imaging: From classical to adjoint tomography, *Tectonophysics*, **566–567**, 31–66, doi: 10.1016/j.tecto.2012.07.006.

Liu, Q. & Tromp, J., 2008. Finite-frequency sensitivity kernels for global seismic wave propagation based upon adjoint methods, *Geophys. J. Int.*, **174**, 265–286, doi: 10.1111/j.1365–246X.2008.03798.x.

Liu, Q., Beller, S., Lei, W., Peter, D. & Tromp, J., 2022. Pre-conditioned BFGS-based uncertainty quantification in elastic full-waveform inversion, *Geophys. J. Int.*, **228**(2), 796–815, doi: 10.1093/gji/ggab375.

Lu, C., Grand, S. P., Lai, H. & Garnero, E. J., 2019. TX2019slab: A new *P* and *S* tomography model incorporating subducting slabs, *J. Geophys. Res.*, **124**(11), 11549–11567, doi: 10.1029/2019JB017448.

Lu, Q. & Rudolph, M. L., 2024. A synoptic view of mantle plume shapes enabled by virtual reality, *Geochem. Geophys. Geosys.*, **25**(6), e2024GC011517, doi: 10.1029/2024GC011517.

Maggi, A., Tape, C., Chen, M., Chao, D. & Tromp, J., 2009. An automated time-window selection algorithm for seismic tomography, *Geophys. J. Int.*, **178**(1), 257–281, doi: 10.1111/j.1365–246X.2009.04099.x.

Maguire, R., Ritsema, J., van Keken, P. E., Fichtner, A. & Goes, S., 2016. *P*- and *S*-wave delays caused by thermal plumes, *J. Geophys. Res.*, **206**(2), 1169–1178, doi: 10.1093/gji/ggw187.

Maguire, R., Ritsema, J., Bonnin, M., van Keken, P. E. & Goes, S., 2018. Evaluating the resolution of deep mantle plumes in teleseismic traveltime tomography, *J. Geophys. Res.*, **123**(1), 384–400, doi: 10.1002/2017JB014730.

Masson, Y. & Romanowicz, B., 2017. Box tomography: localized imaging of remote targets buried in an unknown medium, a step forward for understanding key structures in the deep earth, *Geophys. J. Int.*, **211**(1), 141–163, doi: 10.1093/gji/ggx141.

McNutt, M. K., 1998. Superswells, *Rev. Geophys.*, **36**(2), 211–244, doi: 10.1029/98RG00255.

McNutt, M. K. & Fischer, K. M., 1987, The South Pacific superswell, in *Seamounts, Islands, and Atolls*, edited by B. H. Keating, P. Fryer, R. Batiza, & G. W. Boehlert, vol. 43 of **Geophysical Monograph**, pp. 25–34, doi: 10.1029/GM043, Amer. Geophys. Union.

McNutt, M. K. & Judge, A. V., 1990. The Superswell and mantle dynamics beneath the South Pacific, *Science*, **248**(4958), 969–975, doi: 10.1126/science.248.4958.969.

Mégnin, C. & Romanowicz, B., 2000. The three-dimensional shear velocity structure of the mantle from the inversion of body, surface and higher-mode waveforms, *Geophys. J. Int.*, **143**(3), 709–728, doi: 10.1046/j.1365–246X.2000.00298.x.

Montagner, J.-P. & Anderson, D. L., 1989. Petrological constraints on seismic anisotropy, *Phys. Earth Planet. Inter.*, **54**, 82–105.

Monteiller, V., Beller, S., Plazolles, B. & Chevrot, S., 2020. On the validity of the planar wave approximation to compute synthetic seismograms of teleseismic body waves in a 3-D regional model, *Geophys. J. Int.*, **224**(3), 2060–2076, doi: 10.1093/gji/ggaa570.

Montelli, R., Nolet, G., Dahlen, F. A. & Masters, G., 2006. A catalogue of deep mantle plumes: New results from finite-frequency tomography, *Geochem. Geophys. Geosys.*, **7**(11), Q11007, doi: 10.1029/2006GC001248.

Morgan, W. J., 1971. Convection plumes in the lower mantle, *Nature*, **230**(5288), 42–43, doi: 10.1038/230042a0.

Moulik, P. & Ekström, G., 2016. The relationships between large-scale variations in shear velocity, density, and compressional velocity in the Earth's mantle, *J. Geophys. Res.*, **121**, 2737–2271, doi: 10.1002/2015JB012679.

Moulik, P., Lekić, V., Romanowicz, B., Ma, Z., Schaeffer, A., Ho, T., Beucler, E., Debayle, E., Deuss, A., Durand, S., Ekström, G., Lebedev, S., Masters, G., Priestley, K., Ritsema, J., Sigloch, K., Trampert, J. & Dziewonski, A. M., 2022. Global reference seismological data sets: multimode surface wave dispersion, *Geophys. J. Int.*, **228**(3), 1808–1849, doi: 10.1093/gji/ggab418.

Nolet, G., Karato, S.-I. & Montelli, R., 2006. Plume fluxes from seismic tomography, *Earth Planet. Sci. Lett.*, **248**(3–4), 685–699, doi: 10.1016/j.epsl.2006.06.011.

Nolet, G., Allen, R. & Zhao, D., 2007. Mantle plume tomography, *Chemical Geology*, **241**(3–4), 248–263, doi: 10.1016/j.chemgeo.2007.01.022.

Nolet, G., Hello, Y., van der Lee, S., Bonnieux, S., Ruiz, M. C., Pazmino, N. A., Deschamps, A., Regnier, M. M., Font, Y., Chen, Y. J. & Simons, F. J., 2019. Imaging the Galápagos mantle plume with an unconventional application of floating seismometers, *Sci. Rep.*, **9**, 1326, doi: 10.1038/s41598–018–36835–w.

Obayashi, M., Yoshimitsu, J., Nolet, G., Fukao, Y., Shiobara, H., Sugioka, H., Miyamachi, H. & Gao, Y., 2013. Finite frequency whole mantle *P* wave tomography: Improvement of subducted slab images, *Geophys. Res. Lett.*, **40**(21), 5652–5657, doi: 10.1002/2013GL057401.

Park, J. & Levin, V., 2002. Seismic anisotropy: Tracing plate dynamics in the mantle, *Science*, **296**, 485–489.

Pipatprathanporn, S. & Simons, F. J., 2024. Waveform modeling of hydroacoustic teleseismic earthquake records from autonomous MERMAID floats, *Geophys. J. Int.*, **239**(1), 136–154, doi: 10.1093/gji/ggae238.

Plattner, A. & Simons, F. J., 2015. High-resolution local magnetic field models for the Martian South Pole from Mars Global Surveyor data, *J. Geophys. Res.*, **120**, 1543–1566, doi: 10.1002/2015JE004869.

Rawlinson, N., Fichtner, A., Sambridge, M. & Young, M. K., 2014. Seismic tomography and the assessment of uncertainty, *Adv. Geophys.*, **55**, 1–76, doi: 10.1016/bs.agph.2014.08.001.

Ritsema, J. & Lekić, V., 2020. Heterogeneity of seismic wave velocity in Earth's mantle, *Annu. Rev. Earth Pl. Sc.*, **48**, 377–401, doi: 10.1146/annurev–earth–082119–065909.

Ritsema, J., Rivera, L. A., Komatitsch, D., Tromp, J. & van Heijst, H.-J., 2002. Effects of crust and mantle heterogeneity on PP/P and SS/S amplitude ratios, *Geophys. Res. Lett.*, **29**(10), 1430, doi: 10.1029/2001GL013831.

Ritsema, J., McNamara, A. K. & Bull, A. L., 2007. Tomographic filtering of geodynamic models: Implications for model interpretation and large-scale

mantle structure, *J. Geophys. Res.*, **112**, B01303, doi: 10.1029/2006JB004566.

Ritsema, J., A. Deuss, A., van Heijst, H. J. & Woodhouse, J. H., 2011. S40RTS: a degree-40 shear-velocity model for the mantle from new Rayleigh wave dispersion, teleseismic traveltime and normal-mode splitting function measurements, *Geophys. J. Int.*, **184**, 1223–1236, doi: 10.1111/j.1365–246X.2010.04884.x.

Ritsema, J., Maguire, R., Cobden, L. & Goes, S., 2021, Seismic imaging of deep mantle plumes, in *Mantle Convection and Surface Expressions*, edited by H. Marquardt, M. Ballmer, S. Cottaar, & J. Konter, vol. 263 of **Geophysical Monograph**, chap. 14, pp. 353–369, doi: 10.1002/9781119528609.ch14, Amer. Geophys. Union, Washington, D. C.

Romanowicz, B., 2023, Global seismic tomography using time domain waveform inversion, in *Applications of Data Assimilation and Inverse Problems in the Earth Sciences*, edited by A. Ismail-Zadeh, F. Castelli, D. Jones, & S. Sanchez, Special Publications of the International Union of Geodesy and Geophysics, pp. 220—238, doi: 10.1017/9781009180412.015, Cambridge Univ. Press, Cambridge, UK.

Ronchi, C., Iacono, R. & Paolucci, P. S., 1996. The "Cubed Sphere": A new method for the solution of partial differential equations in spherical geometry, *J. Comput. Phys.*, **124**, 93–114, doi: 10.1006/jcph.1996.0047.

Ruan, Y., Lei, W., Modrak, R., Örsvuran, R., Bozdağ, E. & Tromp, J., 2019. Balancing unevenly distributed data in seismic tomography: a global adjoint tomography example, *Geophys. J. Int.*, **219**(2), 1225–1236, doi: 10.1093/gji/ggz356.

Rudolph, M. L., Lekić, V. & Lithgow-Bertelloni, C., 2015. Viscosity jump in Earth's mid-mantle, *Science*, **350**(6266), 1349–1352, doi: 10.1126/science.aad1929.

Sawade, L., Beller, S., Lei, W. & Tromp, J., 2022. Global centroid moment tensors in a heterogeneous earth: the CMT3D catalogue, *Geophys. J. Int.*, **231**(3), 1727–1738, doi: 10.1093/gji/ggac280.

Schuberth, B. S. A., Bunge, H.-P. & Ritsema, J., 2009. Tomographic filtering of high-resolution mantle circulation models: Can seismic heterogeneity be explained by temperature alone?, *Geochem. Geophys. Geosys.*, **10**(5), Q05W03, doi: 10.1029/2009GC002401.

Shen, Y., Wolfe, C. J. & Solomon, S. C., 2003. Seismological evidence for a mid-mantle discontinuity beneath Hawaii and Iceland, *Earth Planet. Sci. Lett.*, **214**(1–2), 143–151, doi: 10.1016/S0012–821X(03)00349–2.

Shephard, G. E., Matthews, K. J., Hosseini, K. & Domeier, M., 2017. On the consistency of seismically imaged lower mantle slabs, *Sci. Rep.*, **7**(1), 10976, doi: 10.1038/s41598–017–11039–w.

Sigloch, K. & Mihalynuk, M. G., 2013. Intra-oceanic subduction shaped the assembly of Cordilleran North America, *Nature*, **496**(7443), doi: 10.1038/nature12019.

Simon, J. D., Simons, F. J. & Irving, J. C. E., 2021. A MERMAID miscellany: Seismoacoustic signals beyond the *P* wave, *Seismol. Res. Lett.*, **92**(6), 3657–3667, doi: 10.1785/0220210052.

Simon, J. D., Simons, F. J. & Irving, J. C. E., 2022. Recording earthquakes for tomographic imaging of the mantle beneath the South Pacific by autonomous MERMAID floats, *Geophys. J. Int.*, **228**, 147–170, doi: 10.1093/gji/ggab271.

Simons, F. J., van der Hilst, R. D., Montagner, J.-P. & Zielhuis, A., 2002. Multimode Rayleigh wave inversion for heterogeneity and azimuthal anisotropy of the Australian upper mantle, *Geophys. J. Int.*, **151**(3), 738–754, doi: 10.1046/j.1365–246X.2002.01787.x.

Slack, P. D., Fox, C. G. & Dziak, R. P., 1999. *P* wave detection thresholds, P_n velocity estimates, and *T* wave location uncertainty from oceanic hydrophones, *J. Geophys. Res.*, **104**(B6), 13061–13072, doi: 10.1029/1999JB900112.

Sleep, N. H., 1990. Hotspots and mantle plumes: Some phenomenology, *J. Geophys. Res.*, **95**(B5), 6715–6736, doi: 10.1029/JB095iB05p06715.

Steinberger, B., 2000. Plumes in a convecting mantle: Models and observations for individual hotspots, *J. Geophys. Res.*, **105**(B5), 11127–11152, doi: 10.1029/1999JB900398.

Su, J., Houser, C., Hernlund, J. W. & Deschamps, F., 2023. Tomographic filtering of shear and compressional wave models reveals uncorrelated variations in the lowermost mantle, *Geophys. J. Int.*, **234**, 2114–2127, doi: 10.1093/gji/ggad190.

Sukhovich, A., Irisson, J.-O., Perrot, J. & Nolet, G., 2014. Automatic recognition of *T* and teleseismic *P* waves by statistical analysis of their spectra: An application to continuous records of moored hydrophones, *J. Geophys. Res.*, **119**(8), 6469–6485, doi: 10.1002/2013JB010936.

Sukhovich, A., Bonnieux, S., Hello, Y., Irisson, J.-O., Simons, F. J. & Nolet, G., 2015. Seismic monitoring in the oceans by autonomous floats, *Nat. Commun.*, **6**, 8027, doi: 10.1038/ncomms9027.

Tarantola, A., 1986. A strategy for nonlinear elastic inversion of seismic reflection data, *Geophysics*, **51**(10), 1893–1903, doi: 10.1190/1.1442046.

Tarantola, A., 2005. *Inverse problem theory and methods for model parameter estimation*, SIAM, Philadelphia, Penn.

Trabant, C., Hutko, A. R., Bahavar, M., Karstens, R., Ahern, T. & Aster, R., 2012. Data products at the IRIS DMC: Stepping stones for research and other applications, *Seismol. Res. Lett.*, **83**(5), 846–854, doi: 10.1785/0220120032.

Tromp, J., Tape, C. & Liu, Q., 2005. Seismic tomography, adjoint methods, time reversal and banana-doughnut kernels, *Geophys. J. Int.*, **160**(1), 195–216, doi: 10.1111/j.1365–246X.2004.02453.x.

Tsekhmistrenko, M., Sigloch, K., Hosseini, K. & Barruol, G., 2021. A tree of Indo-African mantle plumes imaged by seismic tomography, *Nature Geosci.*, **14**(8), 612–619, doi: 10.1038/s41561–021–00762–9.

Valentine, A. P. & Trampert, J., 2012. Data space reduction, quality assessment and searching of seismograms: autoencoder networks for waveform data, *Geophys. J. Int.*, **189**(2), 1183–1202, doi: 10.1111/j.1365–246X.2012.05429.x.

Valentine, A. P. & Trampert, J., 2015. The impact of approximations and arbitrary choices on geophysical images, *Geophys. J. Int.*, **204**(1), 59–73, doi: 10.1093/gji/ggv440.

Valentine, A. P. & Woodhouse, J. H., 2010. Reducing errors in seismic tomography: combined inversion for sources and structure, *Geophys. J. Int.*, **180**(2), 847–857, doi: 10.1111/j.1365–246X.2009.04452.x.

van der Hilst, R. D., Engdahl, E. R. & Spakman, W., 1993. Tomographic inversion of *P*-data and *p*P-data for aspherical mantle structure below the northwest Pacific region, *Geophys. J. Int.*, **115**(1), 264–302, doi: 10.1111/j.1365–246X.1993.tb05603.x.

Wamba, M. D., Montagner, J.-P., Romanowicz, B. & Barruol, G., 2021. Multi-mode waveform tomography of the Indian Ocean upper and mid-mantle around the Réunion hotspot, *J. Geophys. Res.*, **126**, e2020JB021490, doi: 10.1029/2020JB021490.

Wamba, M. D., Montagner, J.-P. & Romanowicz, B., 2023. Imaging deep-mantle plumbing beneath La Réunion and Comores hot spots: Vertical plume conduits and horizontal ponding zones, *Sci. Adv.*, **9**(4), eade3723, doi: 10.1126/sciadv.ade3723.

Wang, Z. & Dahlen, F. A., 1995.   Spherical-spline parameterization of three-dimensional Earth models, *Geophys. Res. Lett.*, **22**(22), 3099–3102, doi: 10.1029/95GL03080.

Webb, S. C. & Crawford, W. C., 2010.   Shallow-water broadband OBS seismology, *B. Seismol. Soc. Am.*, **100**(4), 1770–1778, doi: 10.1785/0120090203.

Weis, D., Harpp, K. S., Harrison, L. N., Boyet, M., Chauvel, C., Farnetani, C. G., Finlayson, V. A., Lee, K. K. M., Parai, R., Shahar, A. & Williamson, N. M. B., 2023.   Earth's mantle composition revealed by mantle plumes, *Nat. Rev. Earth Env.*, **4**, 604–625, doi: 10.1038/s43017–023–00467–0.

Williams, C. D., Mukhopadhyay, S., Rudolph, M. L. & Romanowicz, B., 2019.   Primitive helium is sourced from seismically slow regions in the lowermost mantle, *Geochem. Geophys. Geosys.*, **20**(8), 4130–4145, doi: 10.1029/2019GC008437.

Wolfe, C. J., Solomon, S. C., Laske, G., Collins, J. A., Detrick, R. S., Orcutt, J. A., Bercovici, D. & Hauri, E. H., 2009.   Mantle shear-wave velocity structure beneath the Hawaiian hot spot, *Science*, **326**(5958), 1388–1390, doi: 10.1126/science.1180165.

Yu, C., Day, E. A., de Hoop, M. V., Campillo, M., Goes, S., Blythe, R. A. & van der Hilst, R. D., 2018.   Compositional heterogeneity near the base of the mantle transition zone beneath Hawaii, *Nat. Commun.*, **9**, 1266, doi: 10.1038/s41467–018–03654–6.

Yuan, Y. O., Bozdağ, E., Ciardelli, C., Gao, F. & Simons, F. J., 2019.   The exponentiated phase measurement, and objective-function hybridization for adjoint waveform tomography, *Geophys. J. Int.*, **221**(2), 1145–1164, doi: 10.1093/gji/ggaa063.

Zhang, Z. & Olugboji, T., 2023.   Lithospheric imaging through reverberant layers: Sediments, oceans, and glaciers, *J. Geophys. Res.*, **128**(6), e2022JB026348, doi: 10.1029/2022JB026348.

Zhang, Z., Irving, J. C. E., Simons, F. J. & Alkhalifah, T., 2023.   Seismic evidence for a 100 km mantle discontinuity under the Pacific, *Nat. Commun.*, **14**, 1714, doi: 10.1038/s41467–023–37067–x.

Zhao, D., 2004.   Global tomographic images of mantle plumes and subducting slabs: insight into deep Earth dynamics, *Phys. Earth Planet. Inter.*, **146**(1–2), 3–34, doi: 10.1016/j.pepi.2003.07.032.

Zhu, H., Bozdağ, E., Peter, D. & Tromp, J., 2012.   Structure of the European upper mantle revealed by adjoint tomography, *Nature Geosci.*, **5**(7), 493–498, doi: 10.1038/ngeo1501.